

# Advanced workflow for multi-well tracer test analysis in a geothermal reservoir

Selçuk Erol<sup>a,\*</sup>, Peter Bayer<sup>b</sup>, Taylan Akin<sup>c</sup>, Serhat Akin<sup>a</sup>

<sup>a</sup> Petroleum and Natural Gas Engineering Department, Middle East Technical University, Turkey

<sup>b</sup> Department of Applied Geology, Martin Luther University Halle-Wittenberg, Halle, Germany

<sup>c</sup> Geothermal Application & Research Center, Pamukkale University, Turkey

## ARTICLE INFO

### Keywords:

Analytical model  
Tracer test  
Solute transport  
Anisotropic permeability  
Geothermal

## ABSTRACT

Interpretation of tracer tests in geothermal reservoirs is carried out by fitting the measured data either with simplified two-dimensional (2-D) analytical solutions or with complex numerical models. Available analytical solutions commonly only describe isotropic conditions in 1-D or 2-D, which is generally unsatisfactory to construct realistic reservoir models. Moreover, due to the large spatial and temporal scale of a tracer test in deep reservoirs, the concentration levels measured in the field are relatively low due to dispersion that complicates the assessment of breakthrough curve tailing and residence time. Fitting tracer data with fully resolving 3-D numerical models thus may be more appropriate, but even with a rich set of field data, reliable calibration is often compromised by the high computational effort and data hunger of such models. In this study, an advanced workflow is presented for evaluating tracer test data. Firstly, a 3-D analytical model in which solute transport is considered in anisotropic porous media is developed. Green's function method is applied to obtain a moving line source solution of the convection-dispersion-diffusion equation for solute transport in a 3-D porous medium. In addition, Green's function equation is analytically convoluted with a rectangular pulse function, which represents tracer injection. Secondly, the analytical model results are fitted to the tracer test data by Monte-Carlo simulations to obtain feasible ranges of flow velocities, as well as longitudinal and transversal dispersivities. Finally, the derived parameter values are implemented in a 3-D numerical model to evaluate the solute residence time in a large-scale reservoir. The results applied to field data from the Kızıldere field in Turkey demonstrate that the workflow provides robust estimates of effective parameters from well-to-well data in complex reservoir systems with anisotropic flow paths. Thus, despite the higher effort of applying convolution and stochastic parameter estimation, the preceding analytical step of the workflow substantially eases numerical model set-up.

## 1. Introduction

Management of subsurface reservoirs is essential for sustainable water supply and energy provision. For the characterization of shallow aquifers and deep reservoirs, tracer injection tests are means to inspect fluid flow and transport properties and to understand the connectivity between the wells for optimal reinjection strategies. In particular, in geothermal reservoirs, tracer test analysis is important to predict the cold-front advancement between injection and production wells and energy depletion. Quantitative characterization of flow, transport processes, and interpretation of tracer test data are major challenges in a subsurface reservoir due to the limited expressiveness of geological and geophysical data for hydraulic characterization. Moreover, the

application scale is large and a long-time duration is needed for monitoring the propagation of tracers in-situ. Solute tracer breakthrough curves (BTC) thus reach only low concentrations, and continued dispersion and long solute residence time cause substantial tailing of BTCs. To deal with these challenges in the analysis, a new workflow is presented to quantify reservoir flow parameters and to improve the assessment of solute tailing behavior in a geothermal reservoir.

The tracer transport process can be scrutinized with computer-based models, with which crucial reservoir parameter values are derived by calibration with field responses. Mostly, analytical models based on solutions of the convection-dispersion-diffusion differential equation are employed (Bullivant and O'Sullivan, 1989; Maloszewski & Zuber, 1993; Gerke and van Genuchten, 1996; Akin, 2001; Becker and Shapiro, 2003; Cihan and Tyner 2011; Houseworth et al., 2013; Somogyvári and Bayer,

\* Corresponding author

E-mail address: [selerol@metu.edu.tr](mailto:selerol@metu.edu.tr) (S. Erol).

<https://doi.org/10.1016/j.geothermics.2022.102375>

Received 2 August 2021; Received in revised form 10 December 2021; Accepted 11 February 2022

Available online 16 February 2022

0375-6505/© 2022 Elsevier Ltd. All rights reserved.

Nomenclature			
$c$	solute concentration ( $\text{mg m}^{-3}$ )	$v$	seepage velocity ( $\text{m s}^{-1}$ )
$c_L$	injected solute concentration rate per meter ( $\text{mg m}^{-1} \text{s}^{-1}$ )	$v_{Tx,y,z}$	solute velocity ( $\text{m s}^{-1}$ )
$C_L$	injected solute concentration rate ( $\text{mg s}^{-1}$ )	$x, y, z$	coordinates (m)
$d$	pore diameter (m)	<i>Greek symbols</i>	
$D_{x,y,z}$	hydrodynamic dispersion coefficient ( $\text{m}^2 \text{s}^{-1}$ )	$\alpha_L$	longitudinal dispersivity (m)
$h$	fracture aperture (m)	$\alpha_T$	transverse dispersivity (m)
$H$	Heaviside step function (i)	$\delta$	Dirac delta function (i)
$H$	line source length (m)	$\Delta P$	pressure difference (Pa)
$K$	distribution coefficient ( $\text{m}^3 \text{kg}^{-1}$ )	$\Delta z$	distance difference in $z$ direction (m)
$L$	characteristic length (m)	$\kappa_{x,y,z}$	absolute permeability ( $\text{m}^2$ )
$L_{av}$	average distance between two points in 3-D (m)	$\mu$	dynamic viscosity (Pa s)
$P$	pressure (Pa)	$\rho$	bulk rock density ( $\text{kg m}^{-3}$ )
$Pe$	Peclet number (i)	$\phi$	porosity (-)
$R$	solute retardation factor (i)	<i>Subscripts</i>	
$s$	zero-order source or production term ( $\text{mg m}^{-3} \text{s}^{-1}$ )	$f$	fracture
$u_{x,y,z}$	flow velocity ( $\text{m s}^{-1}$ )	$inj$	injection
$t$	time (s)	$m$	matrix
$T$	period of rectangular pulse injection (s)	$pro$	production
$T$	temperature (K)		

2017; Ronchetti et al., 2020; Li et al., 2021; Delbar and Chapuis, 2021). There exists a range of different analytical models, which are used individually or imposed into artificial neural network models (Akin, 2005; Gudmundsdottir and Horne 2020; Bodin 2020).

A common assumption for analytical models is one-dimensional (1-D) or 2-D radial symmetry. Models in lower dimensions provide relatively limited isotropic information for intricate porous and fractured media. When tracer tests are conducted during production from large-scale geothermal reservoirs, often multiple wells are operated during tracer injection yielding a flow field with components of forced, non-radial convection. For example, Gunderson et al. (2002) observed that injected tracers flow at significantly oblique angles to the predominant pressure gradient, indicating strong anisotropic reservoir permeability. As an alternative to radial analytical simulation, full 3-D numerical models can be applied at the expense of substantial computational effort and increased data requirements (Cihan and Tyner 2011; Egert et al., 2020; Deb et al., 2020; Wu et al., 2021). Ideally, as a suitable compromise, a 3-D analytical model that accounts for anisotropic permeability and dispersivity would be needed, while keeping the data hunger and thus the computational effort of implementation and calibration low. The development of such a model is the focus of this study.

Analytical solutions of the convection-dispersion-diffusion equation can be obtained through the implementation of different mathematical techniques such as Laplace and Fourier transforms. These are then used to derive transport equations (e.g., van Genuchten and Alves, 1982; Maloszewski and Zuber, 1985; Leij et al., 1993; Yadav and Roy, 2018; Ding et al., 2021) where different methods such as the Fourier series (Güven et al., 1984; Bharati et al., 2019), finite integral transforms (e.g., Cleary and Adrian, 1973) and Green's function method (e.g., Cole et al., 2010; Ellsworth and Butters 1993; Leij et al., 2000; Rivera et al., 2016a; Rivera et al., 2016b) can be applied. Particularly, Green's function method is appropriate to solve the transport equation with arbitrary initial or boundary value profiles in several dimensions for irregular geometries (Greenberg, 1971).

Sauty (1980) presented models for slug and continuous injection of tracers in 1-D uniform and 2-D radial flow conditions in porous media. These models can be used to analyze field data using simple curve matching techniques. Van Genuchten & Alves (1982) are among the pioneers who developed various pulse tracer injection models of solute transport in porous media for convection-dispersion-diffusion processes with Laplace transform techniques applied to semi-infinite and finite

systems (van Genuchten and Alves, 1982; van Genuchten, 1985; van Genuchten and Dalton, 1986). Van Genuchten (1985) derived a shape factor for rock matrix blocks for 1-D convection-dispersion transport. Maloszewski & Zuber (1985) proposed an analytical model of tracer injection in parallel fractures for short-term and long-term tracer experiments. Bullivant & O'Sullivan (1989) developed several 1-D models for tracer transport assuming single fracture, fracture/matrix, dual-porosity cubes, pseudo-steady-state double-porosity, and two fracture conditions. They concluded that the models, which allow transient diffusion from fractures into the surrounding rock matrix (i.e., fracture/matrix and dual porosity cubes approaches), provide a better match to test results than a model, which allows only longitudinal dispersion (i.e., single fracture approach) or a pseudo-steady-state double-porosity approach.

Cihan & Tyner (2011) presented 2-D radial analytical solutions for tracer injection in an infinite dual-porosity medium, which were derived for three conditions: constant injection, instantaneous release, and pulse release. The governing equations were solved by the Laplace transform method for solute concentration as a function of space and time. The solutions were successfully validated with numerical simulations, including matrix advection in longitudinal and transverse directions, and longitudinal dispersion. Houseworth et al. (2013) proposed mathematical models for 2-D flow and transport through a water-saturated single fracture and permeable rock matrix. A Laplace transform method was used to solve these equations. The models are developed for different flow systems as: i) 2-D flow is assumed in the matrix with an arbitrary flow direction relative to the orientation of a fracture; ii) a point source-release of a solute that can take place either in the matrix or fracture; iii) independent longitudinal dispersion and diffusion which may occur either in the fracture or matrix, respectively. A model that considers a divergent radial advective-dispersive transport in fractures and diffusive mass transfer in matrix blocks of rock was introduced by Haddad et al. (2014). Their results revealed that dispersivity is independent of the rock matrix block size distribution for dispersion-dominated transport in the fractures. Bharati et al. (2019) proposed a pulse-type source of an analytical solution of the advection-dispersion equation, where spatially dependent concave and convex dispersivity was obtained with a fractal distribution by using Fourier series.

There exists an analytical 3-D advection-dispersion equation, which was derived by using Green's function method for constant flux

boundary condition evaluated with Laplace transform (Ellsworth and Butters, 1993). This equation accounts for anisotropic flow but neglects dispersivity. Leij et al. (2000) introduced solutions with the Green's function method applied for various solute transport phenomena in infinite, semi-infinite, and finite media. These solutions were applied for conditions with longitudinal and transversal solute transport and a persistent source.

In the present study, a 3-D analytical model is developed. This analytical model can be used for anisotropic media to obtain effective parameters from well-to-well data in particular where flow paths between injection and production wells are complex. Green's function method is applied in 3-D to deal with the solute transport in a medium with a rectangular pulse injection source representative for tracer injection tests. Green's function is solved for anisotropic media by relying on the moving line source theory (Molina et al., 2011a; 2011b). For pulse injection, the approach involves analytical convolution between a rectangular injection function and Green's function of 3-D solute transport.

Overall, this study aims to propose an advanced workflow of tracer test analysis to characterize the conditions in a deep geothermal reservoir. The workflow is specifically tailored to identify anisotropic reservoir parameters and to inspect solute residence time distribution. In the first step, the developed analytical model is coupled with stochastic Monte-Carlo simulations and iteratively fitted to tracer breakthrough data collected at the Kızıldere geothermal field production wells located in the Denizli and Aydın provinces of western Turkey at the eastern part of Büyük Menderes graben (Şimşek et al., 2005). Following that, the derived flow parameter values are used to estimate the anisotropic permeabilities of the reservoir. In most cases, due to dispersion and mixing in the reservoir, the measured tracer concentration in observation wells is very low. After the peak concentration arrival, it is difficult to estimate the solute residence time distribution from the measured solute concentration. The approach presented here thus identifies feasible parameter ranges rather than trying to estimate deterministic values. Moreover, in the last step, the derived anisotropic permeabilities and dispersivities are implemented in a 3-D numerical double-porosity simulator to set up a flexible deep geothermal reservoir model to evaluate the BTC tailing behavior and solute residence time in a large-scale reservoir. The proposed workflow reduces computational expense and time to evaluate reliable values of effective reservoir parameters.

## 2. Methodology

The workflow of this study is shown in Fig. 1. A conceptual geological model based on field measurements and observations is constructed. Then Monte-Carlo simulations are carried out with the analytical model developed here to assess the flow and reservoir parameters by fitting the measured tracer BTCs. In the last step, the injection and production rates, the injection amount of tracer, initial and boundary conditions with the obtained parameters are implemented in a 3-D numerical model to create a local geothermal reservoir model of the Kızıldere field to assess BTC tailing and correspondingly the solute residence time distribution.

### 2.1. Analytical model

For simulation, we first consider a continuous medium. This serves as a basis for the description of transport in porous media and, subsequently, also upscaled conditions in fractured reservoirs. The governing partial differential equation (PDE) of the solute convection-dispersion-diffusion in 3-D cartesian coordinates in porous media is given as:

$$R \frac{\partial c}{\partial t} = \left( D_x \frac{\partial^2 c}{\partial x^2} + D_y \frac{\partial^2 c}{\partial y^2} + D_z \frac{\partial^2 c}{\partial z^2} \right) - u_x \frac{\partial c}{\partial x} - u_y \frac{\partial c}{\partial y} - u_z \frac{\partial c}{\partial z} + s \quad (1)$$

in which  $t$  is time,  $c$  is the solute concentration,  $R$  is the solute

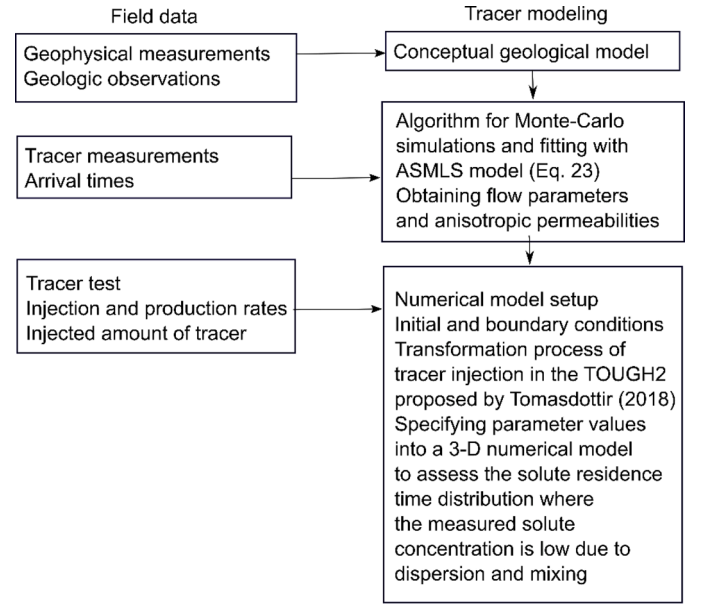


Fig. 1. Workflow of multi-well tracer test analysis conducted in a geothermal reservoir.

retardation factor,  $D_x, y, z$  are hydrodynamic dispersion coefficients,  $u_x, u_y$  and  $u_z$  are flow velocities along the  $x$ -,  $y$ -, and  $z$ -directions, and  $s$  is the production term. The solute retardation can be estimated as:

$$R = 1 + \rho \frac{K}{\phi} \quad (2)$$

where  $\rho$  is bulk rock density,  $K$  is the distribution coefficient and  $\phi$  is the porosity of the porous or fractured medium. Hydrodynamic dispersion coefficients are calculated based on longitudinal  $\alpha_L$  and transverse  $\alpha_T$  dispersivities that are defined in  $x$ -,  $y$ -, and  $z$ -directions as follows:

$$D_x = D_0 + \alpha_L u_x; D_y = D_0 + \alpha_T u_y; D_z = D_0 + \alpha_T u_z \quad (3)$$

in which  $D_0$  is the molecular diffusion coefficient. The dispersivities depend on the velocity field. The  $x$ -direction is considered longitudinal, and  $y$ - and  $z$ -directions are transversal. The diffusion coefficient for an injected liquid tracer at different temperatures can be defined using the Stokes-Einstein equation. The diffusion coefficient of a tracer in a reservoir thus is estimated as:

$$D_{T_2} = D_{T_1} \frac{\mu_{T_2} T_2}{\mu_{T_1} T_1} \quad (4)$$

where  $T_1$  and  $T_2$  are injection and reservoir temperatures, respectively.  $D_{T_1}$  is the diffusion coefficient of a tracer at the injection temperature,  $\mu_{T_1}$  and  $\mu_{T_2}$  are the dynamic viscosity coefficients corresponding to the respective temperatures.

Leij et al. (2000) provide the application of Green's function method on the governing solute convection-dispersion equation (Eq. (1)). Green's function method provides the relationship between a line integral around a closed curve and a triple integral over the plane region ( $x, y, z$ ). The corresponding 3-D problem can be expressed in terms of the differential operator  $\Psi$  as:

$$\Psi(c) = \frac{\partial c}{\partial t} - \left( \frac{D_x}{R} \frac{\partial^2 c}{\partial x^2} + \frac{D_y}{R} \frac{\partial^2 c}{\partial y^2} + \frac{D_z}{R} \frac{\partial^2 c}{\partial z^2} \right) + \frac{u_x}{R} \frac{\partial c}{\partial x} + \frac{u_y}{R} \frac{\partial c}{\partial y} + \frac{u_z}{R} \frac{\partial c}{\partial z} = \frac{s}{R} \quad (5)$$

By multiplying Green's function  $Gf$ , an alternative adjoint problem can be obtained:

$$\begin{aligned} \iiint Gf\Psi(c) &= Bc - \text{terms} + \iiint c\Psi^*(Gf) \\ &= \iiint Gf \frac{S}{R} \end{aligned} \quad (6)$$

where  $Bc$ -terms denotes the boundary terms. Then, the differential operator  $\Psi^*$  given in Eq. (6) can be defined as:

$$\Psi^* = -\left(\frac{D_x}{R} \frac{\partial^2 c}{\partial x'^2} + \frac{D_y}{R} \frac{\partial^2 c}{\partial y'^2} + \frac{D_z}{R} \frac{\partial^2 c}{\partial z'^2}\right) - \frac{u_x}{R} \frac{\partial c}{\partial x'} - \frac{u_y}{R} \frac{\partial c}{\partial y'} - \frac{u_z}{R} \frac{\partial c}{\partial z'} - \frac{\partial}{\partial \tau} \quad (7)$$

The integral variables  $(x', y', z', \tau)$  correspond to coordinate variables and time  $t$  ( $x, y, z, t$ ). The differential operator given in Eq. (7) is similar to the partial differential equation (PDE) provided in Eq. (1) excluding the negative time and the velocity vectors. A solution for tracer concentration  $c$  can be obtained from the equivalent problem through the adjoint operator. Green's function method uses the Dirac delta function  $\delta$  (an impulse spike function), which is applicable for instantaneous tracer injection. The differential operator on the Green's function  $G_f$  is equal to a four-dimensional Dirac delta function given as follows:

$$\Psi^*(Gf) = \delta(x-x')\delta(y-y')\delta(z-z')\delta(t-\tau) = \delta(x-x')\delta(y-y')\delta(z-z')\delta(t-\tau) \quad (8)$$

The Green's function  $Gf(x, y, z, t; x', y', z', \tau)$  indicates the concentration at  $(x, y, z, t)$  as a result of an instant solute release at the time  $\tau$  for a unit source located at  $(x', y', z')$ . The full expression of the equation solved for an infinite spatial domain can be found in Leij et al. (2000) where the basis of a wide variety of analytical models in multiple dimensions is provided. When solving the equation, the production term  $s$  is assumed as zero in most of the cases.

Green's function  $Gf$  is defined as the sum of the fundamental solution  $F$  according to the superposition principle. The fundamental solution  $F$  can be derived by solving Eq. (8) with Fourier transformation and then by solving the initial value problems for an instantaneous point source that result in an analytical expression. The fundamental solution  $F$  can be defined as:

$$F(x, y, z, t; x', y', z', \tau) = F_x(x, t; x', \tau)F_y(y, t; y', \tau)F_z(z, t; z', \tau) \quad (9)$$

Solving the fundamental formulation of the PDE given in Eq. (1), the Green's function  $Gf$  of a pulse point source can be obtained at the given point coordinates  $(x', y', z')$  and time  $t = 0$ . Moreover, applying the moving source theory for the  $x$ -,  $y$ -, and  $z$ -directions with constant drifts (Carslaw and Jaeger, 1959), the fundamental equation can be written as:

$$\begin{aligned} F &= \frac{H(t-\tau)}{\sqrt{D_x D_y D_z \left(\frac{4\pi(t-\tau)}{R}\right)^3}} \\ &\times \exp\left(-\frac{(R(x-x') - v_{Tx}(t-\tau))^2}{4D_x R(t-\tau)} - \frac{(R(y-y') - v_{Ty}(t-\tau))^2}{4D_y R(t-\tau)} - \frac{v_{Tz}^2(t-\tau)}{4D_z R} + \frac{(z-z')v_{Tz}}{2D_z} - \frac{R(z'-z)^2}{4D_z(t-\tau)}\right) \end{aligned} \quad (10)$$

where  $H$  is the Heaviside step function,  $v_{Tx}$ ,  $v_{Ty}$ , and  $v_{Tz}$  are the solute velocities, which yield the flow velocity vector:

$$v_{Tx,y,z} = \frac{Pe_{x,y,z} D_0}{d} = \frac{u_{x,y,z} L}{D_0} \frac{D_0}{d} \quad (11)$$

where  $L$  is the characteristic length,  $d$  is the pore diameter. Eq. (11) is typically defined for porous media. To depict a model from a continuum approach to the fractured medium, a Peclet number based on the

geometric factors of the flow channels can be formulated. It is assumed that a conservative tracer flows with the same velocity as bulk fluid flow. The characteristic length can be calculated as  $L = \pi / Sf$ , where  $Sf$  is the specific surface area.  $Sf$  is the ratio between the cross-section area over a volume of the geometric shape of a spherical pore or for simplicity a cylinder-shaped fracture defined with  $Sf = A / V$ . The Peclet number can be defined as  $Pe_{x,y,z} = u_{x,y,z} L / D_0$ , or for fracture flow  $Pe_{x,y,z} = u_{x,y,z} h / D_0$ , where  $h$  is the fracture aperture.

From this point, the given solution function in Eq. (10) can be integrated along the vertical  $z$ -direction for a finite line source length  $H$  with a pulse of solute injection, where a point source is superpositioned. The solution is expressed as:

$$\begin{aligned} F &= \frac{C_L}{\sqrt{D_x D_y D_z \left(\frac{4\pi t}{R}\right)^3}} \int_0^H \exp\left( \right. \\ &\left. -\frac{(R(x-x') - v_{Tx}t)^2}{4tD_x R} - \frac{(R(y-y') - v_{Ty}t)^2}{4tD_y R} - \frac{v_{Tz}^2 t}{4D_z R} + \frac{(z-z')v_{Tz}}{2D_z} - \frac{R(z'-z)^2}{4tD_z} \right) dz' \end{aligned} \quad (12)$$

where  $C_L$  is solute tracer concentration rate input.

The integration part over the line source length  $H$  in Eq. (10) can be simplified by using the substitution method:

$$\begin{aligned} F &= \frac{C_L}{\sqrt{D_x D_y D_z \left(\frac{4\pi t}{R}\right)^3}} \exp\left(-\frac{(R(x-x') - v_{Tx}t)^2}{4tD_x R} - \frac{(R(y-y') - v_{Ty}t)^2}{4tD_y R}\right) \\ &\times \left( \int_0^H \exp\left(-\frac{v_{Tz}^2}{4D_z R} + \frac{(z-z')v_{Tz}}{2D_z} - \frac{R(z'-z)^2}{4tD_z}\right) dz' \right) \end{aligned} \quad (13)$$

To satisfy the boundary conditions of the domain, the method of images theory is applied on the moving source part in the  $z$ -direction (Bear, 1979), where the source is represented as a line. The substitution part can be represented as:

$$\varphi^2 = \frac{R(z-z')^2}{4D_z t} \rightarrow \varphi = \frac{\sqrt{R}(z-z')}{\sqrt{4D_z t}} \quad (14)$$

$$-\sqrt{\frac{4D_z t}{R}} d\varphi = dz' \quad (15)$$

Integral limits of the  $\varphi$ -value from  $z-H$  to  $z$  and from  $z$  to  $z+H$  are defined to satisfy the boundaries concerning the method of images:

$$\varphi : \frac{z-H}{\sqrt{\frac{4D_z t}{R}}} \rightarrow \frac{z}{\sqrt{\frac{4D_z t}{R}}} \text{ and } \varphi : \frac{z}{\sqrt{\frac{4D_z t}{R}}} \rightarrow \frac{z+H}{\sqrt{\frac{4D_z t}{R}}} \quad (16)$$

Substituting the conditions Eq. (16) and Eq. (15) into Eq. (13), the solution can be rewritten as:

$$F = \frac{C_L \sqrt{\pi t D_z}}{\sqrt{D_x D_y D_z} \left( \frac{4\pi t}{R} \right)^3} \left[ \exp \left( \frac{(R(x-x') - v_{Tx}t)^2}{4tD_x R} - \frac{(R(y-y') - v_{Ty}t)^2}{4tD_y R} \right) \right] \times \left( \operatorname{erf} \left( \frac{R(H-z) + tv_{Tz}}{\sqrt{4tD_z R}} \right) - \operatorname{erf} \left( \frac{tv_{Tz} - Rz}{\sqrt{4tD_z R}} \right) \right) \quad (17)$$

The integration of exponential function  $f = \exp(-\omega^2)$  is expressed with the error function defined as:

$$\operatorname{erf}(x) = \frac{2}{\sqrt{\pi}} \int_0^x \exp(-\omega^2) d\omega \rightarrow \frac{\sqrt{\pi}}{2} \operatorname{erf}(x) = \int_0^x \exp(-\omega^2) d\omega \quad (18)$$

After simplification, Eq. (17) reduces to:

$$F = \frac{C_L R}{8\pi t \sqrt{D_x D_y}} \exp \left( \frac{(R(x-x') - v_{Tx}t)^2}{4tD_x R} - \frac{(R(y-y') - v_{Ty}t)^2}{4tD_y R} \right) \times \left( \operatorname{erf} \left( \frac{R(H-z) + tv_{Tz}}{\sqrt{4tD_z R}} \right) - \operatorname{erf} \left( \frac{tv_{Tz} - Rz}{\sqrt{4tD_z R}} \right) \right) \quad (19)$$

$C_L$  is still a Heaviside step function where  $C_L(t) = 1$ , for  $t \geq 0$ . If  $C_L$  is superimposed per meter depth for a given time, the input rectangular pulse injection function can be analytically convoluted by shifting over the convection-dispersion-diffusion part of Eq. (19) (impulse response) with a given time interval  $\Delta t$ . Details of this technique for heat transfer are described elsewhere (Erol et al., 2015). Here, it is assumed that the solute concentration rate  $C_L$  is injected at a constant rate per meter depth, which can be estimated by dividing the total injection rate of the solute by the total length of the line source,  $H$ .

Eq. (19) is segregated into two parts:  $c_L$  represents a rectangular pulse function, and the convection-dispersion-diffusion part is expressed as an impulse response function  $I(x, y, z, t)$ . Hence, the following equation can be obtained:

$$c(x, y, z, t) = c_L \frac{R}{8\pi t \sqrt{D_x D_y}} \exp \left( \frac{(R(x-x') - v_{Tx}t)^2}{4tD_x R} - \frac{(R(y-y') - v_{Ty}t)^2}{4tD_y R} \right) \times \left( \operatorname{erf} \left( \frac{R(H-z) + tv_{Tz}}{\sqrt{4tD_z R}} \right) - \operatorname{erf} \left( \frac{tv_{Tz} - Rz}{\sqrt{4tD_z R}} \right) \right) \quad (20)$$

$I(x, y, z, t)$

To apply a pulse injection for a specific time frame, the boundary conditions can be defined as follows:

$$c_L(t) = \begin{cases} c_L & \text{for } t \in [0, T] \\ 0, & \text{otherwise} \end{cases} \quad (21)$$

in which  $T$  is the period of rectangular pulse injection,  $c_L$  is the injected

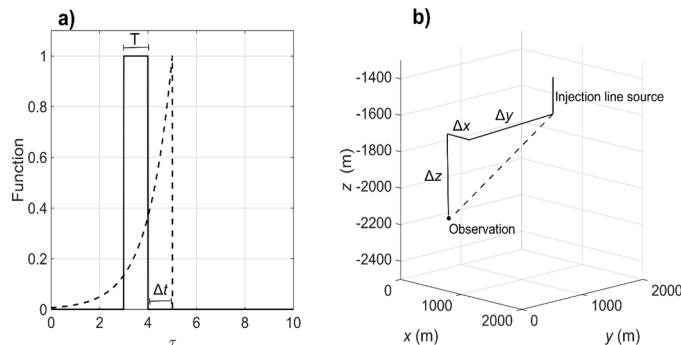


**Fig. 2.** a) Illustration of analytical convolution between impulse response and a rectangular function with a time interval  $\Delta t$ . b) Line source for injection of a tracer and the distance to an observation well in a three-dimensional plane.

tracer concentration rate per meter depth.

The convolution of the function  $I$  and  $c_L$  can be formulated as:

$$c(x, y, z, t) = \int_{-\infty}^{\infty} c_L(\tau) I(x, y, z, t - \tau) d\tau \rightarrow c_L \int_0^T I(x, y, z, t - \tau) d\tau \quad (22)$$

This convolution integral equation can be solved by discretizing both the  $c_L$  and  $I$  function with a differential interval of  $\Delta t$ . The sum of impulse responses at given coordinates  $(x, y, z)$  provides the convolution in analytical form and can be written as:

$$c(x, y, z, t) = \sum_{i=0}^{n-1} c_L(i\Delta t) I(x, y, z, t - i\Delta t) \Delta t \quad (23)$$

where  $i\Delta t$  denote the time interval of each unit impulse (i.e., time delay),  $n$  is the time span, and the delayed and shifted impulse response is expressed as  $c_L(i\Delta t) I(t - i\Delta t) \Delta t$ . For instance, the total amount of injected tracer is 200 kg ( $2 \times 10^8$  mg), which is divided by the assumed line source length (e.g., 150 m). If the time interval is  $\Delta t = 1$  h, then  $2 \times 10^8$  mg /  $H$  is injected per hour. The output concentration is given in  $\text{mg m}^{-3}$ . The coordinates  $x, y, z$  as given in Eq. (20) correspond to the distance difference between the injection and arbitrary observation points ( $\Delta x, \Delta y, \Delta z$ ). The convolution and the line source are illustrated in Fig. 2. The proposed analytical model (Eq. (23)) is called Anisotropic Solute Moving Line Source (ASMLS).

The permeability is estimated according to Darcy's law in 3-D as:

$$\begin{cases} \kappa_x = -\frac{u_x \mu \Delta x}{\Delta P} \\ \kappa_y = -\frac{u_y \mu \Delta y}{\Delta P} \\ \kappa_z = -\frac{u_z \mu \Delta z}{\Delta P} \end{cases} \quad (24)$$

where  $\mu$  is the dynamic viscosity, and  $\Delta P$  is the pressure difference between injection and production wells under steady-state conditions. For the subsequent demonstration, the developed analytical model is implemented in MATLAB version 2019a (MATLAB, 2021).

## 2.2. Models used for comparison and verification

The ASMLS model is compared with four different solutions where different flow conditions are implemented. As the first one, a slug tracer injection model by Sauty (1980) considering advective-dispersive transfer is adopted. This model considers longitudinal and transversal effects of a tracer propagating in a 2-D uniform flow regime. At a given distance from the injection position, the evolution of concentration can be estimated by:



$$C_u = \frac{\alpha_L(\sqrt{(a^2+4)}-2)}{ut} \exp \left[ \frac{(a^2 + (\sqrt{(a^2+4)}-2)^2)}{4(\sqrt{(a^2+4)}-2)} \right] \exp \left[ -\frac{a^2 + \left(\frac{ut}{\alpha_L}\right)^2}{\frac{4ut}{\alpha_L}} \right] \quad (25)$$

where  $u$  is the uniform flow velocity, and  $a$  is given as:

$$a = \sqrt{\frac{x^2}{\alpha_L^2} + \frac{y^2}{\alpha_L \alpha_T}} \quad (26)$$

Bullivant & O'Sullivan (1989) provided several 1-D models for porous and fractured media. Here, two of their models are considered; single fracture and fracture-matrix models. The assumption of the single fracture solution is based on a single flow path where tracer flows within no-slip boundary conditions at the walls of the fracture. The single fracture solution is given as:

$$C_{sf} = \frac{m}{4Q\sqrt{t}} \frac{2t_m}{t} \sqrt{\frac{w}{\pi t_m}} \exp \left( -\frac{w}{4} \frac{(t-t_m)^2}{t_m t} \right) \quad (27)$$

where  $m$  is the total amount of injected tracer,  $Q$  is the mass flow rate,  $t_m = L_{av} / u$  and  $w = uL_{av} / D_{Tr}$ .  $L_{av}$  is the average distance between two points (in this case in 3-D,  $x, y, z$ ).  $D_{Tr}$  is the Taylor dispersion coefficient given as:

$$D_{Tr} = \frac{2}{105} \left( \frac{h}{2} \right)^2 \frac{1}{D_0} \quad (28)$$

In the fracture-matrix model, a large fracture surrounded by rock matrix blocks with micro-fractures is considered. The longitudinal dispersion is ignored to distinguish this model from the single fracture model. The concentration in the observation well can be estimated as:

$$C_{fm} = \frac{mH(t-t_m)}{Q} \sqrt{\frac{t_m}{\pi \frac{u}{L_{av}} \left( \frac{h^2}{D_0 \phi_m} \right)}} \frac{1}{(t-t_m)^{3/2}} \exp \left( -\frac{t_m}{\frac{u}{L_{av}} \left( \frac{h^2}{D_0 \phi_m} \right) (t-t_m)} \right) \quad (29)$$

$\phi_m$  is matrix porosity.  $H(t-t_m)$  is the Heaviside step function.

Welty & Gelhar (1994) proposed four approximate analytical solutions for tracer test analysis. Three solutions developed by Welty & Gelhar (1994) for radial flow and two-well tracer tests do not take into account the flow velocity in the field and require the travel time of the tracer as an input. Only one of the solutions addresses non-uniform flow effects to determine longitudinal dispersivity from tracer tests in aquifers. This solution relies on the variable-velocity conditions of a steady non-uniform flow field and conserves the total mass of the tracer in a stream tube. The equation derived for a pulse input of a tracer mass is given as:

$$C_{WG} = \frac{m_p}{\rho_l v(x_0) \sqrt{4\pi \alpha_L \omega}} \exp \left[ -\frac{\eta^2}{4\alpha_L \omega} \right] \quad (30)$$

$C_{WG}$  is the mass fraction of the tracer,  $m_p$  is the mass of injected tracer per unit cross-sectional area of aquifer,  $\rho_l$  is the density of tracer solution,  $v$  is the seepage velocity,  $x$  is the location,  $\omega$  and  $\eta$  are the integrals that account for the variable dispersion effect as a result of the changing velocity field. The integrals  $\omega$  and  $\eta$  are defined as:

$$\omega = \int_0^{\bar{x}} \frac{1}{v(x)^2} dx \quad (31)$$

$\bar{x}$  is the mean location of the pulse front.

$$\eta = \int_0^{\bar{x}} \frac{1}{v(x)} dx - t \quad (32)$$

As the fifth model used for comparison in the study, a convection-dispersion model by Houseworth et al. (2013) was chosen, which includes variable diffusion and dispersion between matrix and fracture for solute tracer transport:

$$C_H = \frac{C_m}{\sqrt{4\pi \bar{D}^* t}} \sqrt{\bar{D}^* t} \pi \left[ \operatorname{erf} \left( \frac{u_f t - z}{2\sqrt{\bar{D}^* t}} \right) - \operatorname{erf} \left( \frac{u_m t - z}{2\sqrt{\bar{D}^* t}} \right) \right] \quad (33)$$

$u_f$  and  $u_m$  are the flow velocities in fracture and matrix, respectively, and  $C_m = 1$ . The parameter  $z$  can also be specified as the average distance. The time-averaged longitudinal diffusion/dispersion coefficient is:

$$\bar{D}^* = \frac{1}{t} \left( D_f^* \frac{z}{u_f} + D_m^* \left( t - \frac{z}{u_f} \right) \right) \quad (34)$$

in which  $D_f^* = D_L / R_f$  and  $D_m^* = D_L / R_m$ .  $D_L$  is the longitudinal dispersion coefficient,  $R_f$  and  $R_m$  are retardation factors for fracture and matrix, respectively.

### 2.3. Monte-Carlo simulations

In the workflow, we apply the ASMLS model in an exhaustive Monte-Carlo analysis to identify feasible ranges and distributions of anisotropic flow velocities ( $x, y, z$ ), longitudinal and transversal dispersivities. In this analysis, a sufficiently large number of uncertain model parameter values is randomly generated by sampling from predefined distributions. Each sample simulation is tested by computing a square error function to quantify the fitness between the calculated and measured tracer BTCs. Feasible parameter ranges are identified by selecting a set of best-fit results.

In the Monte-Carlo simulations, triangular distributions are assumed in curve analysis, which is a straightforward procedure and nearly approximates a lognormal distribution of a BTC obtained from the tracer test. This is because the triangular distribution provides a continuous and bounded probability in a triangular area providing lower-upper limits and a most likely value such as a lognormal distribution. We defined a triangular probability distribution function as:

$$P_j(i) = P_{j-\min} + X(P_{j-\max} - P_{j-\min}) \quad (35)$$

$P$  is the value of the desired parameter for estimation, bounded with upper and lower limits;  $X$  is the random variable that generates random numbers for each iteration within the range  $0 < X < 1$ . The subscript  $j$  denotes the parameter,  $i$  is the number of realization. The square error function is defined as (Wu et al., 2021):

$$R_j(i) = \frac{1}{\xi_e^2} \left[ \left( \frac{C_{i-peak}}{C_{mea-peak}} - 1 \right)^2 + \left( \frac{t_{i-peak}}{t_{mea-peak}} - 1 \right)^2 + \left( \frac{t_{i,1}}{t_{mea,1}} - 1 \right)^2 + \left( \frac{t_{i,2}}{t_{mea,2}} - 1 \right)^2 \right] \quad (36)$$

the subscript  $i$  denotes the Monte-Carlo simulation results,  $mea$  the measured data,  $peak$  the maximum value of the concentration. The corresponding arrival time is  $t_{peak}$ ;  $t_1$  and  $t_2$  are the beginning and the end of the BTC, respectively. For each realization, we found the beginning and the peak of the BTC. The beginning and the end of the curve are determined in an iterative process. In the first step, a threshold value is set (e.g., 0.1) and concentrations larger than the threshold value are determined. In the second step, the large value differences along the dataset array are evaluated with a special function in MATLAB,  $\text{diff}(c)$ , and the indices of the high difference points on the curve are found as the beginning and the end of the curves. In our application, the end value of the BTC is ignored since the measured tracer data is not (fully)

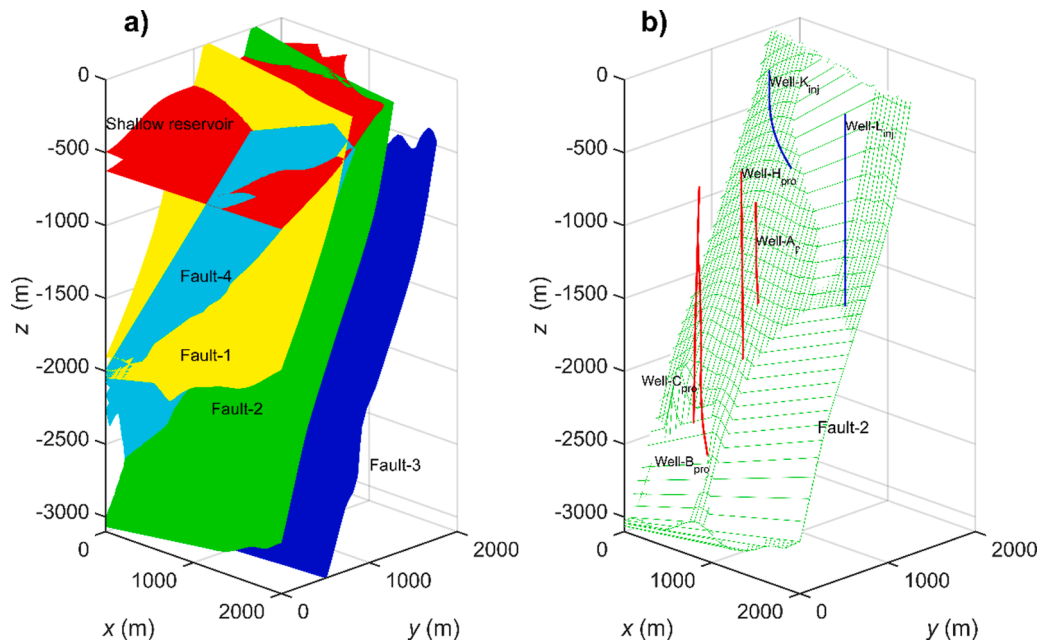


**Fig. 3.** a) Geological settings of the segmented geothermal reservoir of Kizildere. The surface highlighted in red color defines the lower boundary of the shallow reservoir. b) Illustration of the injection (blue) and production (red) wells intersecting fault-2. Tracer is injected into Well-K<sub>inj</sub> and Well-L<sub>inj</sub> and monitored at the production wells (Well-A<sub>pro</sub>, -B<sub>pro</sub>, -C<sub>pro</sub>, and -H<sub>pro</sub>).

available after the peak concentration. There are two major reasons to stop the measurement in the field after the peak arrival time: (i) the concentration that is arrived at some observation wells is low and further concentration recordings are increasingly influenced by dispersion; (ii) the peak arrival time reaches more than a year which is considered a sufficiently long duration for the tracer measurements in the field.

$\xi_e$  is the standard error of the mean that can be estimated as:

$$\xi_e = \frac{\xi}{\sqrt{N}} \quad (37)$$

$\xi$  is the standard deviation of the measurement dataset in dimensionless form ( $c/c_{max}$ ) and  $N$  is the number of measured data.

#### 2.4. Geological settings of case study and field tracer test

The advantages and disadvantages of the ASMLS model are demonstrated with a field tracer test conducted in the Kizildere geothermal field, Turkey. The Kizildere field is bounded by oblique-slip normal faults with various orientations, and more than 80 wells are actively operated. Therefore, managing and ideally avoiding thermal interference and pressure depletion between adjacent wells is of high importance to ensure productivity and long-term sustainability. This study only focuses on a part of the geothermal field where the injection and production activities are intensive. That is why it is of major interest to inspect the existence and relevance of hydraulic connectivity between densely positioned wells. The geological model of the Kizildere geothermal field was constructed based on information gathered from geophysical surveys and borehole data obtained from the wells. Four major faults create a combination of sinks and sources between shallow and deep hydrothermal reservoirs in the region of interest (Fig. 3a). This combination results in various 3-D flow paths in different directions and complicates the estimation of representative reservoir parameters. As shown in Fig. 3b, some of the production and injection wells intersect a single fault zone (Fault-2) where two previous tracer injection tests were performed to explore the connectivity (Akin et al., 2016). The injection was carried out at the shallow wells and monitored from the deeper production wells along the Fault-2. These tracer surveys are suitable to

**Table 1**

Cartesian coordinates of wells where the Fault-2 is approximately intersected, and mean distances from tracer injection wells to the monitoring production wells. The coordinates are based on Fig. 3b.

Well ID	Coordinates (m)			Mean distance to Well-K <sub>inj</sub> , $L_{av}$ (m)	Mean distance to Well-L <sub>inj</sub> , $L_{av}$ (m)
	x (m)	y (m)	z (m)		
Well-K <sub>inj</sub>	750	1140	750		
Well-L <sub>inj</sub>	1810	700	1320		
Well-A <sub>pro</sub>	800	730	1500	880	1025
Well-B <sub>pro</sub>	735	210	2455	1820	1690
Well-C <sub>pro</sub>	500	285	2310	1960	1660
Well-H <sub>pro</sub>	800	550	1750	1270	1150

**Table 2**

Parameter range settings for global sensitivity analysis.

parameter	$u_x$ (m s <sup>-1</sup> )	$u_y$ (m s <sup>-1</sup> )	$u_z$ (m s <sup>-1</sup> )	$\alpha_L$ (m)	$\alpha_T$ (m)
range	$1 \times 10^{-7} - 1 \times 10^{-3}$	$1 \times 10^{-6} - 1 \times 10^{-3}$	$1 \times 10^{-6} - 1 \times 10^{-3}$	1 - 600	0.1 - 250

The number of Monte-Carlo realization points: 50,000.

examine the ASMLS model. For our study, the four production wells located closely to the injection wells were considered.

There are several types of tracer compounds such as traditional tracers like salts (Day 1977; Lei et al., 2010) and dyes (Abrahams et al., 1986; Flury and Wai, 2003), reactive tracers (Leecaster et al., 2012), DNA-tracers (Kong et al. (2018) and thermally sensitive tracers (Hawkins et al., 2017). Often, thermally sensitive tracers such as naphthalene sulfonates, Amino G, and rhodamine WT were applied to evaluate the thermal state of a geothermal system (Rose and Clausen, 2014; 2017). Two types of naphthalene sulfonate compounds, whose thermal decay

**Table 3**

Parameter range settings for local sensitivity analysis following a one-at-a-time principle.

Interested parameter	$u_x$ (m s <sup>-1</sup> )	$u_y$ (m s <sup>-1</sup> )	$u_z$ (m s <sup>-1</sup> )	$\alpha_L$ (m)	$\alpha_T$ (m)
$u_x$	$1 \times 10^{-7}$ - $1 \times 10^{-3}$	$1 \times 10^{-6}$ - $1 \times 10^{-5}$	$1 \times 10^{-6}$ - $1 \times 10^{-5}$	200 - 300	75 - 100
	$1 \times 10^{-5}$ - $1 \times 10^{-3}$	$1 \times 10^{-7}$ - $1 \times 10^{-5}$	$1 \times 10^{-5}$ - $1 \times 10^{-3}$	200 - 300	75 - 100
$u_y$	$1 \times 10^{-5}$ - $1 \times 10^{-3}$	$1 \times 10^{-7}$ - $1 \times 10^{-5}$	$1 \times 10^{-5}$ - $1 \times 10^{-3}$	200 - 300	75 - 100
	$1 \times 10^{-5}$ - $1 \times 10^{-3}$	$1 \times 10^{-7}$ - $1 \times 10^{-5}$	$1 \times 10^{-5}$ - $1 \times 10^{-3}$	200 - 300	75 - 100
$u_z$	$1 \times 10^{-5}$ - $1 \times 10^{-3}$	$1 \times 10^{-7}$ - $1 \times 10^{-5}$	$1 \times 10^{-7}$ - $1 \times 10^{-5}$	200 - 300	75 - 100
	$1 \times 10^{-5}$ - $1 \times 10^{-3}$	$1 \times 10^{-7}$ - $1 \times 10^{-5}$	$1 \times 10^{-7}$ - $1 \times 10^{-5}$	200 - 300	75 - 100
$\alpha_L$	$1 \times 10^{-5}$ - $1 \times 10^{-3}$	$1 \times 10^{-5}$ - $1 \times 10^{-3}$	$1 \times 10^{-5}$ - $1 \times 10^{-3}$	1 - 600	75 - 100
	$1 \times 10^{-5}$ - $1 \times 10^{-3}$	$1 \times 10^{-5}$ - $1 \times 10^{-3}$	$1 \times 10^{-5}$ - $1 \times 10^{-3}$	200 - 300	0.01 - 250
$\alpha_T$	$1 \times 10^{-5}$ - $1 \times 10^{-3}$	$1 \times 10^{-5}$ - $1 \times 10^{-3}$	$1 \times 10^{-5}$ - $1 \times 10^{-3}$	200 - 300	0.01 - 250
	$1 \times 10^{-5}$ - $1 \times 10^{-3}$	$1 \times 10^{-5}$ - $1 \times 10^{-3}$	$1 \times 10^{-5}$ - $1 \times 10^{-3}$	200 - 300	0.01 - 250

The number of Monte-Carlo realization points for each parameter: 5000.

kinetics are suitable for use in reservoirs with temperatures up to 300 °C (Rose et al., 2001, 2002), are used as tracers at Kızıldere. The reservoir temperature is as high as 242 °C at around 2000 m depth (Şimşek, 2003). The tracer compounds, with a mass of 200 kg of 1-naphthalene sulfonate, and the same amount of 1,6-naphthalene disulfonate were separately mixed with the effluent fluid and injected in the injection wells Well-K<sub>inj</sub> and Well-L<sub>inj</sub>, respectively. Both of the tracer injections were completed in less than an hour. In the analytical model, the line source length  $H$  is specified based on the well screen of each injection well and it is assumed that the tracer is uniformly injected along with the fully penetrated well screen. For instance, the total amount of tracer injected in one hour into Well-K<sub>inj</sub> was 200 kg. This amount is simply divided by the well screen of Well-K<sub>inj</sub> as 150 m, which means that  $c_L$  must be specified as  $1.33 \times 10^6$  mg m<sup>-1</sup> h<sup>-1</sup> in the analytical model depending on the time interval in the convolution (i.e., 370 mg m<sup>-1</sup> s<sup>-1</sup>). Similarly, the well screen of Well-L<sub>inj</sub> is 400 m long. The coordinates and the average distances between injection and production wells that were used in calculations are given in Table 1.

In the ASMLS model, there are five unknown parameters (flow velocities in  $x$ -,  $y$ -,  $z$ -directions, and dispersivities) to assess with Monte-Carlo simulations. Firstly, we applied global sensitivity analysis with 50,000 realizations to determine the average ranges of each parameter.

Then, in 5000 realizations, the sensitivity of each parameter was tested following a one-at-a-time principle: the value limits of the concerned parameter were set in a wide range, while those of the other parameters were kept narrow. For instance, the flow velocity in  $x$ -direction was analyzed within the limits from  $1 \times 10^{-7}$  to  $1 \times 10^{-3}$  m s<sup>-1</sup>, while for other parameters such as longitudinal dispersivity a tight limit of 200 to 300 m was set, and the other velocities are bounded between  $1 \times 10^{-6}$  and  $1 \times 10^{-5}$  m s<sup>-1</sup>. The range of the parameters and settings for global sensitivity and the local sensitivity analysis are given in Tables 2 and 3.

The calculation with all 5000 realizations in MATLAB took a computational time of 50 min (Hardware specifications: Intel Core i7-9750H CPU @ 2.60 GHz processor with 16 GB of RAM). The ASMLS model was derived based on the convolution approach in which the impulse of injection is considered with implicit time steps. Therefore, the runtime of each realization is longer compared to applying analytical solutions without convolution.

## 2.5. Numerical model

The numerical model is employed after the analytical analysis to examine the solute residence time distribution in greater detail that is affected by dispersion in a large-scale geothermal reservoir. A 3-D local numerical model is constructed based on the previously prepared geological model (Fig. 3a). In addition to the six wells depicted in Fig. 3b, the neighbor injection and production wells where the tracer test was conducted are also included in the numerical model (Fig. 4b). Heat and mass fluxes obtained from a full field model and affected by wells outside of this local model are implemented at the boundary cells (Erol et al., 2022). For this, the EOS1 flow module of the numerical modeling platform TOUGH2 (2021) is used, which couples flow and solute tracer transport in a non-isothermal system. A fixed-state boundary condition is defined at the top of the model. The model is run until the pressure ( $P$ ) and temperature ( $T$ ) gradients have reached the natural state conditions of the field (e.g., over 100,000 years) and fitted to static measurements obtained from the wells as a function of depth. The preconditioned bi-conjugate gradient is selected as solver and the maximum relative error criterion is set to  $1 \times 10^{-7}$ . A mesh with 39,375 regular grid blocks is generated (Fig. 4a), which allows

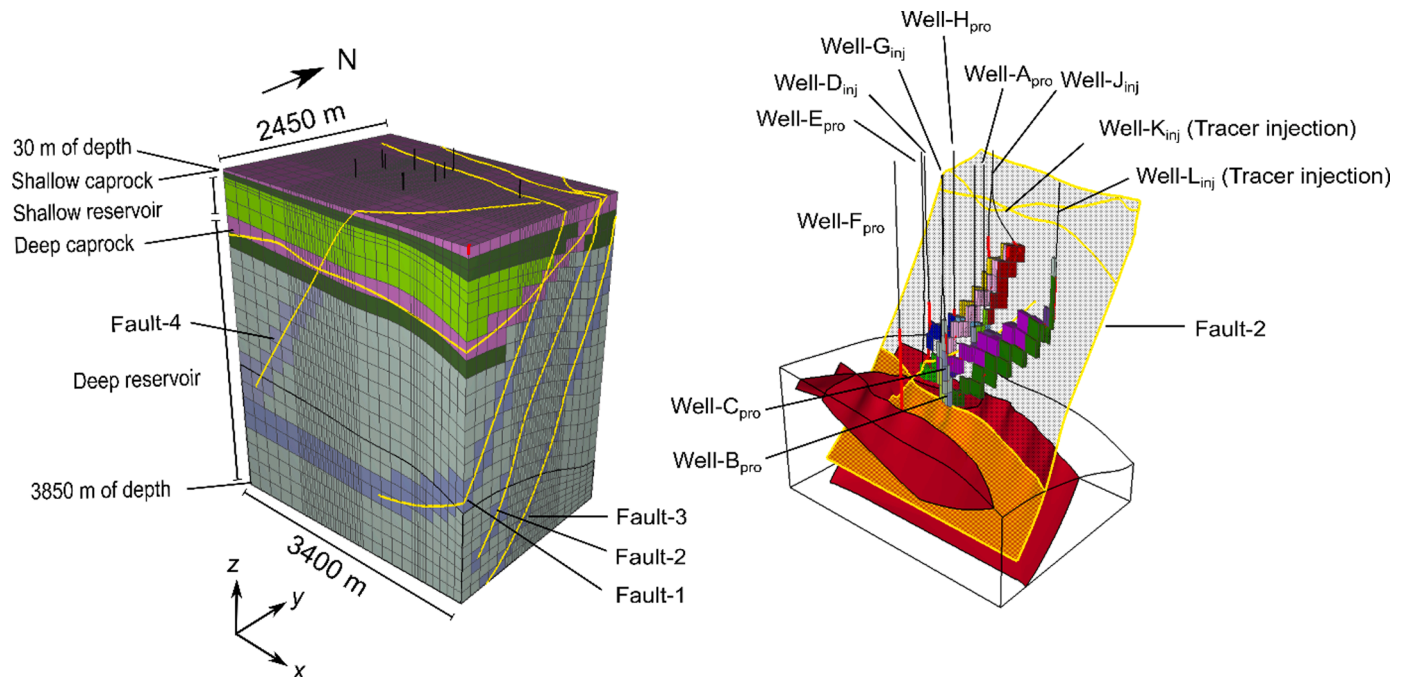


**Fig. 4.** The numerical model setup. a) Illustration of the grid and geological settings. b) The well locations and flow paths are depicted in different colors. Subscript *pro* represents production, and *inj* describes injection.



specifying permeability in three directions ( $x$ ,  $y$ ,  $z$ ), which is more flexible than for example Voronoi grids ( $x$ ,  $y = z$ ). The discretized block area is 1600 m<sup>2</sup> near the wells and expands to 6000 m<sup>2</sup> towards the boundaries. The model is subdivided into 25 layers with variable thicknesses ranging from 40 m to 170 m. Flow paths are created between the wells as shown in Fig. 4b. The matrix permeability in each direction is defined as nearly impermeable as  $1 \times 10^{-16}$  m<sup>2</sup> with a matrix porosity of 0.04. The effective fracture permeability values in  $x$ -,  $y$ -,  $z$ -directions are calibrated and specified based on the velocity field determined from the tracer data-ASMLS model matches.

The multiple interacting continua (MINC) method, which is an improved technique of the dual-porosity model described by Warren & Root (1963), was used for the simulations (Pruess, 1992). For example, Fayer et al. (2009) assessed thermally degrading tracers in injection tests with the MINC method implemented in the TOUGH2 simulator. In the ASMLS model, dispersivities  $\alpha_L$  and  $\alpha_T$  can be obtained by matching field-measured concentrations, but these parameters are not recognized in the TOUGH2 simulator. Therefore, the obtained dispersivities are defined as matrix block sizes in TOUGH2. The longitudinal one in the  $x$ -direction and transverse one in  $y$ - and  $z$ -directions are specified accordingly. The dispersivity does not perfectly correspond to the matrix block scale, but this assumption is expected to alleviate matching between tracer measurements and numerical results. In the following, it is tested whether the numerical dispersion in the TOUGH2 simulator with the MINC approach is suitable to represent the macro-dispersion characterized by the ASMLS model while examining the BTC tailing behavior of the tracer and its residence time distribution.

Here, we assume an equivalent permeability approach for the fractured medium in the ASMLS model. In dual-porosity systems, it is assumed that the fluid flow from the matrix to fractures is in a steady-state condition (Warren and Root 1963). As time goes to infinity, at the end of the flow path both in fracture and matrix, the pressure drops must be identical. Therefore, the fluid flow velocity either in a porous medium or in the fractured medium can be assumed the same. Firstly, the flow velocities are determined with the new analytical model fitting to the tracer data. Following that, the flow velocity is used to estimate the porous permeability with Darcy's law given the pressure difference between the considered wells. Subsequently, this permeability is assumed equivalent to fracture permeability. Thus, the cubic law is applied to estimate the fracture aperture (the porous permeability with Darcy's law = fracture permeability  $k_f = h^3/12$  according to the cubic law). The convection-dispersion-diffusion was assumed to be valid, disregarding some other approaches, which consider more complex transport phenomena in fractured media controlled by fracture geometrical properties, including tortuosity, fracture roughness, and

connectivity.

A sudden pulse tracer injection within a short period (i.e., 200 kg in 15 min) causes convergence problems in TOUGH2, even if the relative tolerance and time step are set to considerably small values (specified time step such as 1 s and relative tolerance of  $1 \times 10^{-7}$ ). Recently, Tómasdóttir (2018) proposed a transformation method that could be used to tackle convergence issues in TOUGH2. According to this approach, the specified tracer injection rate is multiplied with injection time, and the real amount of the tracer injected in the field is divided by the total tracer amount defined in TOUGH2. This ratio is multiplied by the mass fraction of the tracer and the flow rate at the well grids. Using this method, the tracer injection rate in TOUGH2 is specified as  $30 \text{ kg s}^{-1}$  injected in 7000 s ( $7000 \text{ s} \times 30 \text{ kg/s} = 2.1 \times 10^6 \text{ kg}$  injected in the numerical model,  $200 \text{ kg real tracer} / 2.1 \times 10^6 \text{ kg} \rightarrow \lambda = 9.5238 \times 10^{-4}$ ). In the numerical model, the calculated tracer mass fraction,  $\chi$ , and production flow rate in the intersected grid,  $Q$ , is multiplied with the scaling parameter  $\lambda$  to tackle convergence issues due to a large mass of tracer. If the production well intersects multiple grids, the observed tracer concentration can be calculated as  $c = \lambda \sum \chi_i Q_i / \sum Q_i$ , where  $i$  denotes the number of intersected grids.

### 3. Results

In the workflow, we first apply Monte-Carlo simulations with the ASMLS model to determine values for the unknown parameters in the form of distributions. The concentrations are calculated at the point coordinates nearest to the observation well where Fault-2 is intersected (Fig. 3). Fig. 5 shows the scatter plots between parameters and the total misfit of a tracer concentration measurement at the observation Well-A<sub>pro</sub>. The scatter plot of the parameters  $u_x$  and  $\alpha_L$  cover a broad range whereas the feasibility range of  $u_y$  and  $\alpha_T$  are evaluated at a more optimal point. The reason is that Fault-2, where the fluid flow is dominant, intersects Well-K<sub>inj</sub> and Well-A<sub>pro</sub> in the aligned  $y$ -axis. The transversal  $\alpha_T$  and longitudinal dispersivity  $\alpha_L$  are at a clearer feasibility range on the misfit function  $R_{fit}$  due to the dominant vertical flow directions  $u_y$  and  $u_z$  and the vertical heterogeneity. In other wells, we observed similar outputs in that the flow directions of the injection and observation wells are aligned on the vertical axis resulting in the total misfit at a clearer range for the flow velocity  $u_y$  and  $u_z$ .

The ASMLS model results are compared with other approximate solutions by fitting each model with the tracer data injected into Well-K<sub>inj</sub> and measured at Well-A<sub>pro</sub>. The results are plotted in a dimensionless form in Fig. 6. The estimated values of the parameters obtained from the fits for the case where the tracer was injected in Well-K<sub>inj</sub> and monitored

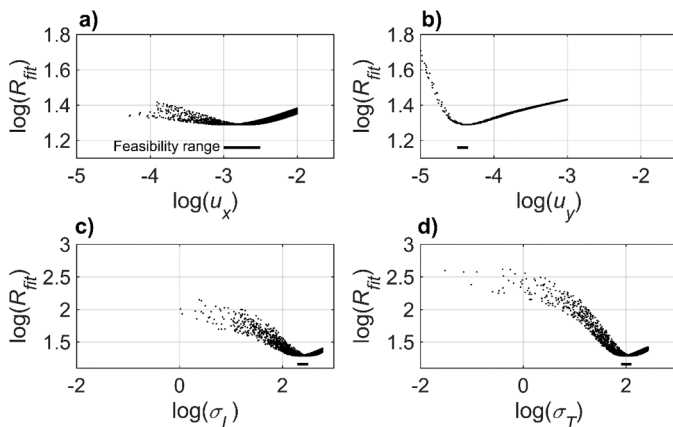


Fig. 5. Monte-Carlo simulation results of the tracer transport (Well-A<sub>pro</sub>). The misfit function  $R_{fit}$  is plotted as a function of the flow velocity in  $x$ - and  $y$ -directions (a and b), longitudinal and transversal dispersivities (c and d). Each point represents a realization. Tracer was injected into Well-K<sub>inj</sub>.

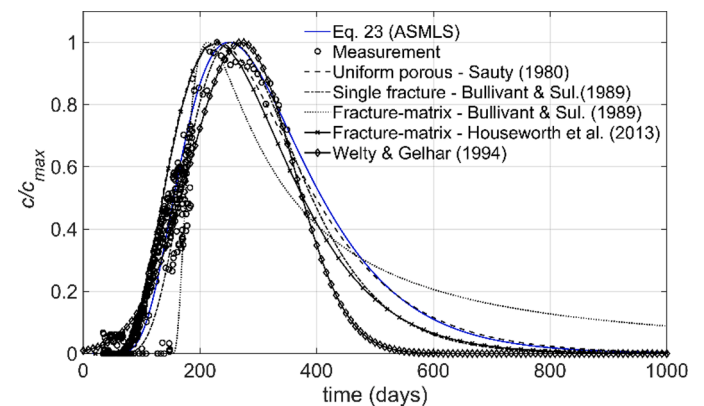


Fig. 6. Analytical models are fitted to measured tracer data (Well-A<sub>pro</sub>). The models used are the ASMLS model (Eq. (23)); the uniform porous medium model, Eq. (25) (Sauty, 1980); the single fracture and fracture-matrix models, Eq. (27) - Eq. (29) (Bullivant and O'Sullivan, 1989); non-uniform flow model Eq. (30) (Welty and Gelhar 1994); and the fracture-matrix model Eq. (33) (Houseworth et al., 2013). Tracer is injected into Well-K<sub>inj</sub>.

**Table 4**

Comparison of parameters obtained by simulating tracer test data in different analytical models.

Analytical models	$\phi$ (i) <sup>a</sup>	$h$ (m) <sup>b</sup>	$u$ (m s <sup>-1</sup> )			Peclet number <sup>c</sup>			$\alpha$ (m)	
			$u_x$	$u_y$	$u_z$	$Pe_x$	$Pe_y$	$Pe_z$	$\alpha_L$	$\alpha_T$
ASMLS model, Eq. (23)	$\phi_f \approx 0.025$	$1 \times 10^{-4}$	$4 \times 10^{-4}$	$3 \times 10^{-5}$	$6 \times 10^{-5}$	13	1.3	2.1	260	$\alpha_L \times 0.4$
Sauty (1980) – uniform porous model, Eq. (25)	–	–	$5.5 \times 10^{-5}$	–	–	$Pe_L = 0.4$ ; $Pe_T = 9$	–	–	150	$\alpha_L \times 0.2$
Bullivant & O'Sullivan (1989) – Single fracture, Eq. (27)	–	$3 \times 10^{-3}$	$3.5 \times 10^{-5}$	–	–	$Pe = 100$	–	–	–	–
Bullivant & O'Sullivan (1989) – fracture-matrix, Eq. (29)	$\phi_m = 0.005$	$3 \times 10^{-3}$	$7 \times 10^{-5}$	–	–	$Pe = 150$	–	–	–	–
Welty & Gelhar (1994), Eq. (30)	$\phi_m = 0.025$	–	$v = u / \phi_m = 0.012$	$u = 3 \times 10^{-4}$	–	–	–	–	$10^4$	–
Houseworth et al. (2013) –fracture-matrix, Eq. (33)	–	$2 \times 10^{-4}$	$u_f = 4.4 \times 10^{-5}$ ; $u_m = 4 \times 10^{-5}$	–	–	$Pe_f = 9$ $Pe_m = 8$	–	–	–	–

<sup>a</sup> Fracture porosity value was taken from Chilingarian et al. (1992) according to the fracture aperture. <sup>b</sup> Fracture aperture was determined based on the cubic law (see Section 2.5). <sup>c</sup>  $Pe_L = \Delta x / \alpha_L$ ,  $Pe_T = \Delta y / (\alpha_L \alpha_T)^{1/2}$ ,  $\Delta x = 62$  m,  $\Delta y = 607$  m.  $Pe_f = u_f h / D_0$ ,  $Pe_m = u_m d / D_0$ ,  $D_0 = 1 \times 10^{-9}$  m<sup>2</sup> s<sup>-1</sup>.

**Table 5**Parameter values were obtained by matching tracer measurements between Well-K<sub>inj</sub> and the production wells with the ASMLS model.

From Well-K <sub>inj</sub> to other wells	$\Delta z$ (m)	$\Delta P$ <sup>a</sup> (MPa)	$R$ (i)	$u$ (m s <sup>-1</sup> )			$\kappa$ (m <sup>2</sup> ) <sup>b</sup>			$\alpha$ (m)	
				$u_x$	$u_y$	$u_z$	$\kappa_x$	$\kappa_y$	$\kappa_z$	$\alpha_L$	$\alpha_T$
Well-A <sub>pro</sub>	750	7	1.65	$4 \times 10^{-4}$	$3 \times 10^{-5}$	$6 \times 10^{-5}$	$6 \times 10^{-13}$	$4 \times 10^{-13}$	$1.3 \times 10^{-12}$	260	$\alpha_L \times 0.4$
Well-H <sub>pro</sub>	1000	8	1.2	$4 \times 10^{-4}$	$2 \times 10^{-5}$	$6 \times 10^{-5}$	$2 \times 10^{-13}$	$3 \times 10^{-13}$	$1.2 \times 10^{-12}$	260	$\alpha_L \times 0.4$
Well-C <sub>pro</sub>	1500	10	1.2	$1.3 \times 10^{-4}$	$2 \times 10^{-4}$	$4 \times 10^{-5}$	$6 \times 10^{-13}$	$3 \times 10^{-12}$	$1 \times 10^{-12}$	260	$\alpha_L \times 0.4$
Well-B <sub>pro</sub>	1600	11	1.2	$4 \times 10^{-4}$	$6.5 \times 10^{-5}$	$6 \times 10^{-5}$	$9 \times 10^{-13}$	$1 \times 10^{-12}$	$1.3 \times 10^{-12}$	260	$\alpha_L \times 0.4$

<sup>a</sup> Values are obtained from the TOUGH2 numerical model after the hydraulic regime has reached steady-state conditions.  $\mu = 0.16 \times 10^{-3}$  at temperature of 230 °C. <sup>b</sup> Absolute permeability calculated with Eq. (24) with the flow velocities. The permeability values were transferred to the TOUGH2 simulator as fracture permeability approximated using the cubic law.

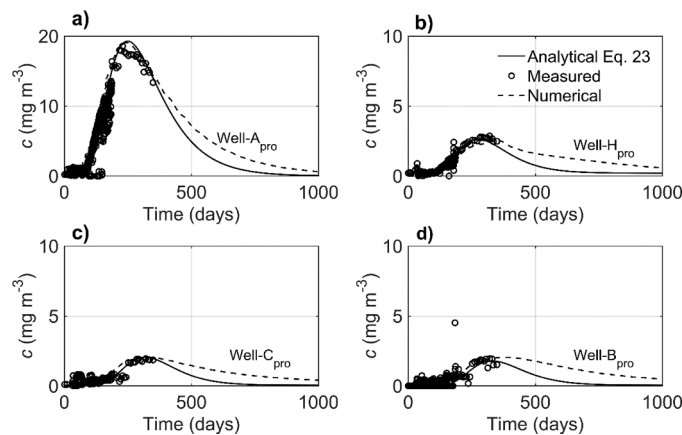


**Fig. 7.** Match between the ASMLS model response (Eq. (23)) and tracer measurements and comparison with the numerical model results. The parameters specified in the numerical model are listed in Table 5. Tracer is injected into Well-K<sub>inj</sub>.

at Well-A<sub>pro</sub> are given in Table 4. The advantages and disadvantages of the analytical models are discussed in Section 4. According to Chilingarian et al. (1992), fracture porosity typically ranges from 0.1% to 3% and they demonstrate a correlation between fracture aperture and fracture porosity. Based on this correlation, we determined the fracture porosity corresponding to the fracture aperture that is evaluated from the cubic law. The fitted models fairly match the field data except for the fracture-matrix model given by Eq. (29) (Fig. 6). The fracture aperture and flow velocity are specified similarly both in the single fracture and fracture-matrix models of Bullivant & O'Sullivan (1989) as shown in Table 4. However, as dispersion is neglected in Eq. (29), the fracture-matrix model shows a sharper peak around the mean arrival time of the tracer compared to the single-matrix model. Instead, the matrix porosity affects the result in this fracture-matrix model. Larger matrix porosity delays the mean arrival time and shifts the tracer concentration over a longer period, whereas smaller matrix porosity causes sudden breakthrough behavior without dispersion but facilitates fitting the mean arrival time.

For further analysis, the analytical ASMLS model is coupled with

Monte-Carlo simulations to fit the measured tracer data monitored in other observation wells in the reservoir shown in Fig. 3b. Eq. (23) is calibrated for each injection and observation well couple separately (e. g., Well-K<sub>inj</sub> to -A<sub>pro</sub>, Well-K<sub>inj</sub> to -B<sub>pro</sub>, etc.). Results are reported in Table 5 and the fits are depicted in Fig. 7. Flow velocities are mainly stimulated by the forced convection between the injection and production (tracer observation) wells. The flow velocity in the x-direction is one order of magnitude faster compared to y- and z-directions, but the observation wells are located in y- and z-axes directions where the velocity is slower. In contrast, we found that absolute permeability is larger in the z-axis direction. The reason is that the pressure gradient is small (i.e., low-pressure gradient). Longitudinal dispersivity value of 260 m with a field-scale of around 2500 m is in accord with the ranges reported by Gelhar et al. (1992) and Neuman (1990) (e.g.,  $\alpha_L = 10^2$  to  $10^3$  m for scales ranging from  $10^3$  to  $10^4$  m).

During the Monte-Carlo application of the ASMLS model, the feasible range is obtained with a transversal dispersivity that is around 0.4 times smaller than the longitudinal dispersivity. According to Gelhar et al. (1992), vertical transverse dispersivity is typically an order of magnitude smaller than longitudinal dispersivity, which however may differ among different field sites. The reason can be attributed to the fractured medium and the oblique-slip fault orientations which are perpendicular to the surface with the dip angle around 45°.

The parameters given in Table 5 are derived with Monte-Carlo simulations by matching the ASMLS model to field data. The obtained values are assigned in the 3-D numerical TOUGH2 model for simulating flow and transport (Fig. 4b) to examine the residence time distribution and to check the consistency of the ASMLS model. The permeability is estimated with Darcy's law based on the evaluated flow velocities. Based on this, the permeability of the porous medium is assumed equivalent to fracture permeability  $\kappa_f = h^3/12$  according to the cubic law.

As depicted in Fig. 7, the tracer is injected into Well-K<sub>inj</sub> located at the northern part of the model. The first and mean arrival times of the numerical results match well with the measured data at the production wells, but the simulation roughly overestimates the tracer amount after the mean arrival time. The dispersion in the numerical model is stronger due to the matrix blocks having a fractal structure. The dispersed and mixed solute tracer continues to reach the production well from the surrounding flow paths, whereas we cannot take into account this effect in the ASMLS model. Therefore, the solute residence time is larger in the

**Table 6**

Results were obtained from fitting the analytical ASMLS model (Eq. (23)) to tracer measurements. Parameters were determined for tracer tests between Well-L<sub>inj</sub> and the production wells listed.

From Well-L <sub>inj</sub> to other wells	$\Delta z$ (m)	$\Delta P^a$ (MPa)	$R$ (i)	$u$ (m s <sup>-1</sup> )			$\kappa$ (m <sup>2</sup> ) <sup>b</sup>			$\alpha$ (m)	
				$u_x$	$u_y$	$u_z$	$\kappa_x$	$\kappa_y$	$\kappa_z$	$\alpha_L$	$\alpha_T$
Well-A <sub>pro</sub>	250	2	1.15	$8 \times 10^{-6}$	$4.5 \times 10^{-5}$	$6.5 \times 10^{-5}$	$6 \times 10^{-13}$	$2 \times 10^{-13}$	$1.3 \times 10^{-12}$	260	$\alpha_L \times 0.4$
Well-H <sub>pro</sub>	600	6	1.15	$8 \times 10^{-6}$	$5.5 \times 10^{-5}$	$9 \times 10^{-5}$	$2 \times 10^{-13}$	$3 \times 10^{-13}$	$1.5 \times 10^{-12}$	260	$\alpha_L \times 0.4$
Well-C <sub>pro</sub>	1000	8	1.15	$1.4 \times 10^{-5}$	$1.3 \times 10^{-4}$	$4 \times 10^{-5}$	$3 \times 10^{-13}$	$1 \times 10^{-12}$	$8 \times 10^{-13}$	260	$\alpha_L \times 0.4$
Well-B <sub>pro</sub>	1100	10	1.15	$1.1 \times 10^{-5}$	$1.4 \times 10^{-4}$	$4.5 \times 10^{-5}$	$2 \times 10^{-13}$	$1 \times 10^{-12}$	$8 \times 10^{-13}$	260	$\alpha_L \times 0.4$

<sup>a</sup> Values are obtained from the TOUGH2 numerical model while pressure difference reaches steady-state conditions.  $\mu = 0.16 \times 10^{-3}$  at 230 °C temperature. <sup>b</sup> Absolute permeability is calculated with Eq. (24) as explained in Table 5.

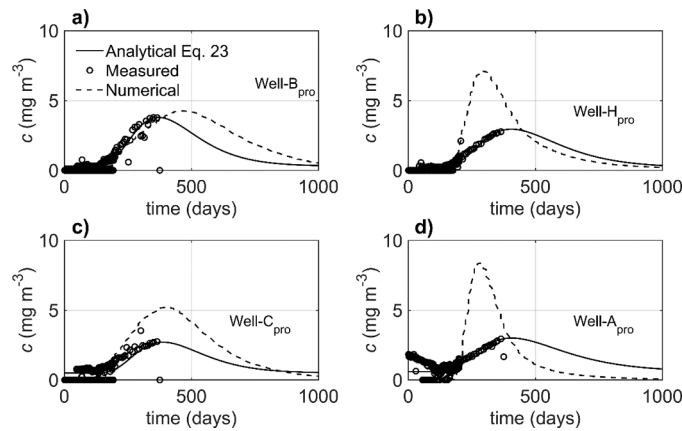


**Fig. 8.** Fitting between the analytical ASMLS model response (Eq. (23)) and tracer measurements, and comparison to the numerical model results. The parameters specified in the numerical model can be found in Table 6. Tracer is injected into Well-L<sub>inj</sub>.

numerical model. Further sensitivity analysis with the numerical model revealed that the specified fracture porosity has an impact on the tracer amount obtained at the production well. Smaller fracture porosity

causes faster fluid flow velocity due to a larger pressure gradient. Therefore, the tracer front-advection is more dominant and a larger peak is observed. In contrast, larger fracture porosity decreases the fluid flow velocity and the tracer disperses through matrix blocks. This hampers the detection of a clear peak in the BTC. The matrix permeability has a minor impact on the mean arrival time because the advection is predominant through fractures and the arrival time of the tracer is not affected.

Furthermore, tracer BTCs observed in production wells as a result of tracer injection into Well-L<sub>inj</sub> located in the eastern part of the field are analyzed (Fig. 3). For this case, the evaluated parameters obtained from the Monte-Carlo simulations are reported in Table 6. In particular, permeability values are in line with the values for the first injection case shown in Table 5. The wells A<sub>pro</sub> and H<sub>pro</sub> are located at shallower depths compared to the deeper wells, B<sub>pro</sub> and C<sub>pro</sub>. As a result,  $\kappa_y$  is larger at a shallower depth (1000 m to 1500 m) and slightly decreases at the deeper reservoir sections (2000 m to 3000 m). In contrast to  $\kappa_y$ ,  $\kappa_z$  shows opposite behavior at identical depths compared to Table 5. Drill cuttings and well-log data show that quartzite-schist is found at some shallower and deeper sections of the reservoir. These formations contain platy minerals such as muscovite laminations that may act as barriers and enhance the anisotropy of the permeability with increasing shear stress of the faults (Zhang et al., 1999; Almquist et al., 2011).

The permeability values given in Table 6 are specified in the TOUGH2 numerical model using the aforementioned simulation

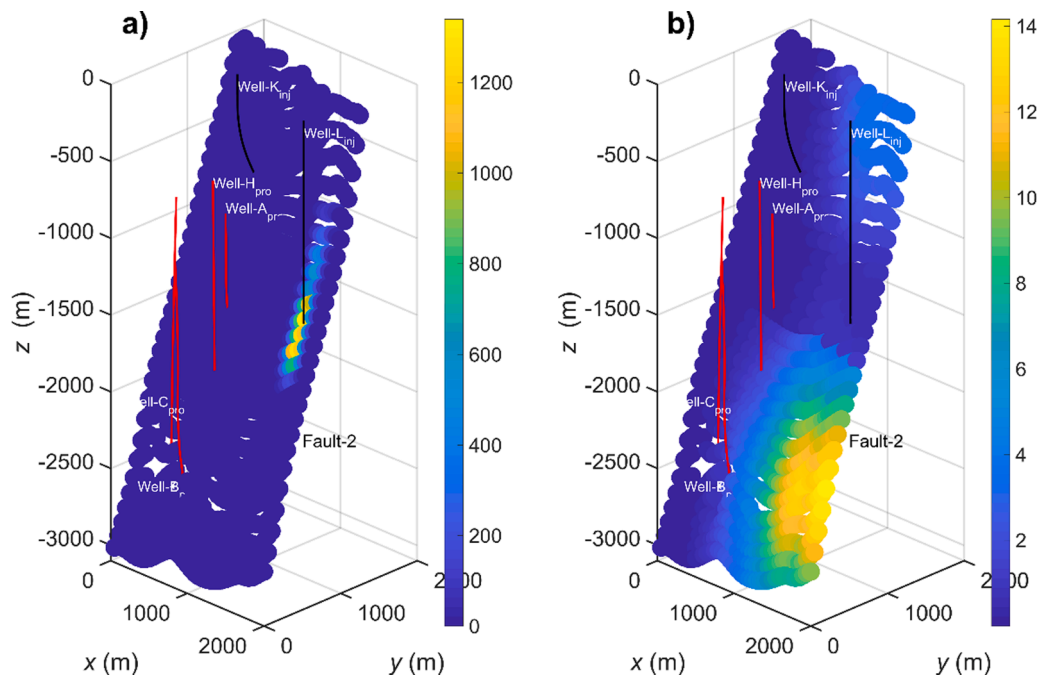


**Fig. 9.** Injected tracer amount along Fault-2 calculated with the analytical ASMLS model (in mg m<sup>-3</sup>). a) Results after 10 days of injection. b) Results 300 days after tracer is released. 200 kg of tracer is released from Well-L<sub>inj</sub> (400 m screen length considered for the line source). Mean flow velocities are specified according to Table 6 as above 1500 m depth:  $u_x = 8 \times 10^{-6}$ ,  $u_y = 5 \times 10^{-5}$ ,  $u_z = 7 \times 10^{-5}$ ; below 1500 m depth:  $u_x = 1 \times 10^{-5}$ ,  $u_y = 1 \times 10^{-4}$ ,  $u_z = 4 \times 10^{-5}$ .

procedure. The matrix properties are specified identical as in the previous case. The results of the numerical model demonstrated in Fig. 8 for the Well-L<sub>inj</sub> injection case show delayed and shifted arrival of the peak at Well-B<sub>pro</sub>, most likely due to the dispersed solute tracer through cross-flow paths between matrix blocks and leading to longer solute residence time distribution. This indicates that rendering the macro-dispersivity values obtained from the ASMLS model by the numerical model by block sizes is not appropriate due to the conceptual numerical assumptions. Moreover, Fig. 8 also shows that the peak concentration is overestimated at Wells H<sub>pro</sub> and A<sub>pro</sub>. The distance is closer between these wells and Well-L<sub>inj</sub> compared to Well-B<sub>pro</sub> and Well-C<sub>pro</sub>. Here, the advection dominates the flow along a preferential path with a minor contribution from dispersion, causing a faster transport and larger tracer concentration observed at the production wells. Due to low dispersion, the solute residence time observed at Wells H<sub>pro</sub> and A<sub>pro</sub> is short.

These discrepancies between the measured and numerical results can also be attributed to the injection transformation method in the TOUGH2 simulator, proposed by Tómasdóttir (2018) mentioned in Section 2.4, may have an impact on the mean arrival times due to a longer injection period in the numerical model (i.e., 7000 s). New developments in conditional stochastic transport modeling (Wu et al., 2021) and multiscale or hierarchical geostatistical modeling (Bodin 2020) may overcome this inconsistency in fractured reservoirs but requires large computational expense.

The tracer transport visualized in Fig. 9 shows how the injected tracer is dispersed at different time frames along Fault-2 calculated with the proposed ASMLS model. The tracer is injected into Well-L<sub>inj</sub> and propagates mainly in the z-axis along the deeper part of Fault-2. After 10 days of tracer injection, the largest tracer amount is calculated around 1200 mg m<sup>-3</sup> that has moved approximately 200 m to the deeper reservoir sections (Fig. 9a). The tracer plume is spread through Fault-2 after 300 days at which the mean arrival time is detected for the tracer at the observation wells. The tracer plume where the largest tracer amount is calculated around 14 mg m<sup>-3</sup> at the center, penetrates through the deeper parts of the reservoir (Fig. 9b).

#### 4. Discussion

The workflow employs an analytical model coupled with Monte-Carlo simulations for characterizing complex geothermal reservoirs. The ASMLS model provides an anisotropic flow field triggered by forced convection between injection and production wells, whereas other approximations assume uniform or non-uniform flow velocities. Specifically, Sauty's uniform porous model gives dispersivity values. Compared to the ASMLS model, the longitudinal and transverse dispersivities are relatively small in Sauty's approximation. The reason can be attributed to the reduced dimensional flow, which may lead to a smaller apparent 2-D dispersivity. The model of Welty & Gelhar (1994) accounts for the variable-velocity conditions of a flow field, but the direction of the flow is still uniform. In other words, the flow velocity varies in a single direction. Compared to the other models, the dispersivity value obtained from the solution of Welty & Gelhar (1994) is two orders of magnitude larger. The reason is that the integration of flow velocity over distance (Eq. (31) and Eq. (32)) has an impact on the dispersion that is evaluated. As the distance increases in the field (e.g., 1000 m distance between the wells), the dispersion value significantly increases with the model developed by Welty & Gelhar (1994). The model of Houseworth et al. (2013) is based on separated flow mechanisms both in fracture and matrix. However, the fit of tracer data is achieved with similar flow velocities in fracture and matrix. When compared to the model of Bullivant & O'Sullivan (1989), the fracture aperture is one order of magnitude larger and Eq. (34) takes into account dispersion and retardation through fracture and matrix, which yields an increase of the tracer arrival time ( $\bar{D}^*$  in Eq. (34) becomes  $3 \times 10^{-3} \text{ m}^2 \text{ s}^{-1}$ ). Comparison of Peclet numbers indicates that the transversal

propagation is stronger in Sauty's model. Roubinet et al. (2012), who inspected the transverse dispersion effect in a 2-D fracture-matrix flow, demonstrated that the longitudinal diffusion in the matrix is crucial at low Peclet numbers, whereas the transverse dispersion in fractures has a minor impact on solute transport. However, Sauty's approximation to estimate Peclet number ( $Pe_L = \Delta x / \alpha_L$ ,  $Pe_T = \Delta y / (\alpha_L \alpha_T)^{-1/2}$ ) is based on the given coordinates that are specified rather than actual fracture aperture or equivalent pore diameter. Aside from this, Peclet numbers calculated using the proposed analytical ASMLS model show similarities in opposite directions between  $Pe_x \approx Pe_T$  and  $Pe_y \approx Pe_L$  due to dimensional differences in calculations. All of the aforementioned approximations provide similar uniform flow velocities, which correspond to the flow velocities in the y- and z-direction, with the observation well located on flow axes of y and z in the proposed model. The dispersivity is an additional parameter facilitating accurate matches with the measured data.

The ASMLS model provides similar outputs but has some major advantages such as evaluation of anisotropic flow velocities and allowing pulse tracer injections into multi-well systems in which the duration of the injection can also be adjusted. In contrast to other analytical solutions, the calculation of the ASMLS model is somewhat larger due to the convolution technique in which the unit impulse (i.e., tracer injection) was convoluted explicitly over time. As the required time interval becomes smaller, the runtime of the convolution takes longer. For instance, fitting a tracer test measurement for one year with an hour time interval takes three seconds for each stochastic random variable. This is a disadvantage for statistical Monte-Carlo simulations in which the analysis may consist of thousands of realization values to determine a confident interval for unknown parameters.

The use of the ASMLS model for fractured media application is only feasible when the hydraulic conditions can be similarly described by an equivalent porous media. We assumed an upscaled equivalent with respect to the Peclet number, and the macro-dispersivity reflects scale effects of heterogeneous media (Gelhar et al., 1979). This is supported by Neuman (1994; 2008) indicating that the volume-averaged fractured rock properties exhibit similarities to that of porous media. In addition, Neuman (1987; 2005) and others (Ando et al., 2003; Neuman and Di Federico, 2003) suggest that flow and transport equations developed for the fractured rocks are amenable to the equations derived for porous media. In contrast, Zech et al. (2015) state that available scale laws are quite arbitrary, and fractured rocks cannot be defined by Fickian laws. However, Neuman (2016) points out that the data sets used by Zech et al. (2015) for small-scale values are not sufficient to demonstrate a dispersivity scale effect. Still, there exists no consensus on representative anisotropies and scaling behavior of dispersivities employed in convection-dispersion-diffusion-based models (Park and Lee, 2021; Tang and Zee, 2021). A major role for the non-univocal observations is played by the diversity of geological conditions.

The comparison between macro-dispersivity and the numerical dispersivity in the numerical simulation with the MINC approach demonstrates that the numerical dispersion parameters with the nested matrix blocks to represent the macro-dispersion of a tracer are not relevant. In the numerical model, dynamic flow factors such as low-permeability transition zones between fracture and matrix blocks and preferential flow paths dominantly control the transport process of the tracer that affect the results. The matrix-fracture functions are based on the geometry of the matrix and fractures (i.e., square blocks in the MINC approach) that are lumped to a factor called the shape factor (Rostami et al., 2020). Perhaps, different geometries and shape factors of matrix-fracture systems provide better consistency between macro-dispersivity and numerical dispersivity in fractured porous media simulations.

#### 5. Conclusions

A new workflow for the analysis of a tracer test conducted in a



geothermal reservoir is presented. In the workflow, a 3-D analytical model for tracer injection is developed to inspect solute transport in an anisotropic medium. A Monte-Carlo simulation algorithm is then coupled to determine optimal values for unknown reservoir parameters. The estimated parameters are used in a more complex numerical model to evaluate the solute residence time in a large-scale reservoir and benchmark the numerical dispersion against macro-dispersion.

The ultimate purpose of this workflow is to characterize the course of energy depletion in a geothermal reservoir, thus the impact of reservoir cooling on the production, and to support optimization of long-term injection strategies.

Embedded in the presented workflow, the ASMLS model is based on Green's function method to facilitate a moving line source of the convection-dispersion-diffusion equation for solute transport. Afterward, the derived equation is analytically convoluted with a rectangular function of a pulse, which solves the equation in a given period. This convolution technique can provide flexibility to model multiple tracer injections from several wells in a given time. Several solute tracer transport approximations reported in the literature are analyzed and compared with the proposed analytical model. The results demonstrate that independent of the model type (e.g., uniform porous, fracture-matrix, etc.), analytical approaches can be used to determine reservoir parameters representative of the Kizildere geothermal site. However, these approximations provide uniform and non-uniform flow parameters, which are not adequate to inform a fully-resolving 3-D numerical model for detailed geothermal reservoir characterization. This is overcome by the new ASMLS model that yields robust fundamental parameter values such as those of flow velocities, longitudinal and transversal dispersivities in systems. In addition, Monte-Carlo simulations help to quantify parameters.

For the construction of the 3-D numerical model, the evaluated parameters, longitudinal and transverse dispersivities, obtained from the analytical model, are used to specify the length, width, and height of matrix blocks in a simulated dual porosity system (i.e., the MINC approach). Two injection cases from different wells are considered to scrutinize solute residence time distribution. In the first case, the injected solute tracer mixes and considerably disperses in the numerical model due to the matrix blocks having a fractal structure. Therefore, the solute residence time is larger in the numerical model. In the second case, the injected tracer reaches the production wells, which are close to the injection well, with a larger peak concentration and the solute residence time distribution is short indicating that dispersion is less significant. These comparisons of the two injection cases do not show any significant relationship between dispersivity and the matrix block sizes. Therefore, dispersivity can be considered separately. This also demonstrates that the mechanical macro-dispersion cannot reliably be represented by numerical dispersion. The transition between matrix and fractures described with block geometries and its defined shape factors most likely affect the results in the numerical simulations. Different geometries and shape factors of matrix-fracture systems may overcome this inconsistency. Alternative concepts of stochastic transport modeling and multiscale-hierarchical geostatistical modeling may support examining various geometries and shape factors of those systems to evaluate correct numerical dispersion system equivalent to macro-dispersion.

The presented workflow represents an integrated approach to acquiring possible effective parameters from well-to-well tracer data while reducing the computational effort and ambiguity to assess geothermal reservoir characteristics. It is most suitable for tests conducted in reservoirs where significant parameter anisotropy prevails, and forced convection between the injection and production wells is dominant. The workflow follows a stochastic procedure to determine reliable value ranges of unknown parameters. This is crucial for setting up a more comprehensive numerical model to analyze the solute residence time distribution, which could be further improved with a more detailed geological or geostatistical conceptualization. The ASMLS model provides promising estimations of dual-porosity systems under

steady-state conditions. In contrast, its applicability to dynamic dual-permeability would be limited.

To interpret reactive tracer applications, the analytical model developed here accounts for retardation. The retardation factor implemented in the model can for instance quantify the effect of sorption of biochemical organic tracers. Moreover, for nonconservative tracers, the reaction part of the solute transport equation can be implemented to take into account first-order decay. (Eq. 2-5, 9, 12, 14, 18, 21, 22, 26, 28, 35, 37)

## Data availability statement

Corresponding data is uploaded to the Mendeley repository

Contact: selerol@metu.edu.tr

Program language: MATLAB

Software required: TOUGH2 simulator

Data size: 17 MB

Measurement datasets, appropriate computer code, and numerical models used in this manuscript are available in the following link: <https://data.mendeley.com/datasets/mr2fw9dyhv/4>

## Declaration of Competing Interest

The authors declare that they have no known competing financial interests or personal relationships that could have appeared to influence the work reported in this paper.

## Acknowledgments

This paper presents the results of the GECO Project, funded by the European Union's Horizon 2020 research and innovation program under grant agreement No. 818169. We would like to thank the two anonymous reviewers for their constructive comments, and Ryan Pearson for proofreading. The authors would like to thank ZORLU Energy for the tracer data.

## Supplementary materials

Supplementary material associated with this article can be found, in the online version, at [doi:10.1016/j.geothermics.2022.102375](https://doi.org/10.1016/j.geothermics.2022.102375).

## References

- Abrahams, A.D., Parsons, A.J., Luk, S.-H., 1986. Field measurement of the velocity of overland flow using dye tracing. *Earth Surf. Proc. Land.* 11 (6), 653–657. <https://doi.org/10.1002/esp.3290110608>.
- Almqvist, B.S.G., Mainprice, D., Madonna, C., Burlini, L., Hirt, A.M., 2011. Application of differential effective medium, magnetic pore fabric analysis, and X-ray microtomography to calculate elastic properties of porous and anisotropic rock aggregates. *J. Geophys. Res.* 116, B01204. <https://doi.org/10.1029/2010JB007750>.
- Ando, K., Kostner, A., Neuman, S.P., 2003. Stochastic continuum modeling of flow and transport in a crystalline rock mass: fanay-Augeres, France, revisited. *Hydrogeol. J.* 11 (5), 521–535. <https://doi.org/10.1007/s10040-003-0286-0>.
- Akin, S., 2001. Analysis of tracer tests with simple spreadsheet models. *Comput. Geosci.* 27, 171–178. [https://doi.org/10.1016/S0098-3004\(00\)00084-4](https://doi.org/10.1016/S0098-3004(00)00084-4) doi.org/.
- Akin, S., 2005. Tracer model identification using artificial neural networks. *Water Resour. Res.* 41, W10421. <https://doi.org/10.1029/2004WR003838>.
- Akin, S., Güney, A., Şentürk, E., Şengün, R., Kılıncarslan, S., 2016. Tracer testing at kizildere geothermal field, turkey, using naphtalene sulfonates. In: *Proceedings, 41st Workshop on Geothermal Reservoir Engineering Stanford University, Stanford, California, February 22-24, 2016, SGP-TR-209*.
- Bear, J., 1979. *Hydraulics of Groundwater*. McGraw-Hill, New York, US. ISBN-10: 0486453553.
- Becker, M.W., Shapiro, A.M., 2003. Interpreting tracer breakthrough tailing from different forced-gradient tracer experiment configurations in fractured bedrock. *Water Resour. Res.* 39, 39. <https://doi.org/10.1029/2001WR001190>.
- Bharati, V.K., Singh, V.P., Sanskrityayn, A., Kumar, N., 2019. Analytical solution for solute transport from a pulse point source along a medium having concave/convex spatial dispersivity within fractal and Euclidean framework. *J. Earth Syst. Sci.* 128, 203. <https://doi.org/10.1007/s12040-019-1231-5> doi.org/.
- Bodin, J., 2020. MFIT 1.0. 0: multi-flow inversion of tracer breakthrough curves in fractured and karst aquifers. *Geosci. Model Develop.* 13 (6), 2905–2924. <https://doi.org/10.5194/gmd-13-2905-2020>.

- Bullivant, D.P., O'Sullivan, M.J., 1989. Matching a field tracer test with some simple models. *Water Resour. Res.* 25 (8), 1879–1891. [doi.org/10.1029/WR025i008p01879](https://doi.org/10.1029/WR025i008p01879).
- Carslaw, H.S., Jaeger, J.C., 1959. *Conduction of Heat in Solids*, 2nd Edition. Oxford University Press, New York, US. ISBN-9780198533030.
- Chilingarian, G.V., Mazzullo, S.J., Rieke, H.H., (1992), Carbonate reservoir characterization: a geologic-engineering analysis, part I, p. 639.
- Cleary, R.W., Adrian, D.D., 1973. Analytical solution of the convective-dispersive equation for cation transport in soils. *Soil Sci. Soc. Am., Proceedings* 37, 197–199. [doi.org/10.2136/sssaj1973.03615995003700020014x](https://doi.org/10.2136/sssaj1973.03615995003700020014x).
- Cihan, A., Tyner, J.S., 2011. 2-D radial analytical solutions for solute transport in a dual-porosity medium. *Water Resour. Res.* 47, W04507. <https://doi.org/10.1029/2009WR008969>.
- Cole, K.D., Beck, J.V., Haji-Sheikh, A., Litkouhi, B., 2010. *Heat Conduction Using Green's Functions*, 2nd Edition. Hemisphere Publ., Washington, DC. ISBN-9781439813546.
- Day, T.J., 1977. Observed mixing lengths in mountain streams. *J. Hydrol. (Amst)* 35 (1–2), 125–136. [https://doi.org/10.1016/0022-1694\(77\)90081-6](https://doi.org/10.1016/0022-1694(77)90081-6).
- Delbar, A., Chapuis, R.P., 2021. Tracer movements in a straight uniform flow: new equations for the advective part considering the distortion of flow lines around the well. *J. Contam. Hydrol.* 239, 103776 <https://doi.org/10.1016/j.jconhyd.2021.103776>.
- Deb, P., Knapp, D., Marquart, G., Clauser, C., Trumphy, E., 2020. Stochastic workflows for the evaluation of enhanced geothermal system (EGS) potential in geothermal greenfields with sparse data: the case study of Acoculco, Mexico. *Geothermics* 88, 101879. <https://doi.org/10.1016/j.geothermics.2020.101879>.
- Ding, X.H., Feng, S.J., Zheng, Q.T., 2021. A two-dimensional analytical model for contaminant transport in a finite domain subjected to multiple arbitrary time-dependent point injection sources. *J. Hydrol. (Amst)* 597, 126318. <https://doi.org/10.1016/j.jhydrol.2021.126318>.
- Egert, R., Korzani, M.G., Held, S., Kohl, T., 2020. Implications on large-scale flow of the fractured EGS reservoir Soultz inferred from hydraulic data and tracer experiments. *Geothermics* 84, 101749. <https://doi.org/10.1016/j.geothermics.2019.101749>.
- Erol, S., Hashemi, M.A., François, B., 2015. Analytical solution of discontinuous heat extraction for sustainability and recovery aspects of borehole heat exchangers. *Int. J. Therm. Sci.* 88, 47–58. <https://doi.org/10.1016/j.ijthermalsci.2014.09.007>.
- Erol, S., Akin, T., Başer, A., Saraçoğlu, Ö., Akin, S., 2022. Fluid-CO<sub>2</sub> injection impact in a geothermal reservoir: evaluation with 3-D reactive transport modeling. *Geothermics* 98, 102271. <https://doi.org/10.1016/j.geothermics.2021.102271>.
- Ellsworth, T.R., Butters, G.L., 1993. Three-dimensional analytical solutions to the advection-dispersion equation in arbitrary Cartesian coordinates. *Water Resour. Res.* 29, 3215–3225. <https://doi.org/10.1029/93WR01293> doi.org/.
- Fayer, S., Rose, P., Petty, S., Deo, M.D., Xu, T., 2009. A computational technique for estimating the fracture surface area adjacent to a newly stimulated well within an engineered geothermal system. In: *Proceedings of TOUGH Symposium 2009*, Lawrence Berkeley National Laboratory, Berkeley, California, September 14–16, 2009.
- Flury, M., Wai, N.N., 2003. Dyes as tracers for vadose zone hydrology. *Rev. Geophys.* 41 (1), 1002. <https://doi.org/10.1029/2001RG000109>.
- Gelhar, L.W., Gutjahr, A.L., Naff, R.L., 1979. Stochastic analysis of macrodispersion in a stratified aquifer. *Water Resour. Res.* 15 (6), 1387–1397.
- Gelhar, L.W., Welty, C., Rehfeldt, K.R., 1992. A critical review of data on field-scale dispersion in aquifers. *Water Resour. Res.* 28 (7), 1955–1973. <https://doi.org/10.1029/92WR00607> doi.org/.
- Welty, C., Gelhar, L.W., 1994. Evaluation of longitudinal dispersivity from nonuniform flow tracer tests. *J. Hydrol. (Amst)* 153 (1–4), 71–102. [https://doi.org/10.1016/0022-1694\(94\)90187-2](https://doi.org/10.1016/0022-1694(94)90187-2).
- Gerke, H.H., van Genuchten, M.T., 1996. Macroscopic representation of structural geometry for simulating water and solute movement in dual-porosity media. *Adv. Water Resour.* 19, 343–357. [https://doi.org/10.1016/0309-1708\(96\)00012-7](https://doi.org/10.1016/0309-1708(96)00012-7) doi.org/.
- Greenberg, M.D., 1971. *Application of Green's Functions in Science and Engineering*. Prentice-Hall, Englewood Cliffs, NJ. ISBN-9780130388360.
- Gunderson, R., Parini, M., Sirad-Azwar, L., 2002. Fluorescein and naphthalene sulfonate liquid tracer results at the awibengkok geothermal field, west java, Indonesia. In: *Proceedings 27th Workshop on Geothermal Reservoir Engineering*, Stanford University, CA-US.
- Gudmundsdottir, H., Horne, R.N., 2020. Prediction modeling for geothermal reservoirs using deep learning. In: *Proceedings 45th Workshop on Geothermal Reservoir Engineering* Stanford University, Stanford, California, February 10–12, 2020.
- Güven, O., Molz, F.J., Melville, J.G., 1984. An analysis of dispersion in a stratified aquifer. *Water Resour. Res.* 20, 1337–1354. <https://doi.org/10.1029/WR020i010p01337>.
- Haddad, A.S., Hassanzadeh, H., Abedi, J., Chen, Z., 2014. Application of tracer injection tests to characterize rock matrix block size distribution and dispersivity in fractured aquifers. *J. Hydrol. (Amst)* 510, 504–512. <https://doi.org/10.1016/j.jhydrol.2014.01.008> doi.org/.
- Hawkins, A.J., Fox, D.B., Becker, M.W., Tester, J.W., 2017. Measurement and simulation of heat exchange in fractured bedrock using inert and thermally degrading tracers. *Water Resour. Res.* 53, 1210–1230. <https://doi.org/10.1002/2016WR019617>.
- Houseworth, J.E., Asahina, D., Birkholzer, J.T., 2013. An analytical model for solute transport through a water-saturated single fracture and permeable rock matrix. *Water Resour. Res.* 49, 6317–6338. <https://doi.org/10.1002/wrcr.20497>.
- Kong, X.Z., Deuber, C.A., Kittilä, A., Somogyvári, M., Mikutis, G., Bayer, P., Wendelin, J.S., Saar, M.O., 2018. Tomographic reservoir imaging with DNA-labeled silica nanotracers: the first field validation. *Environ. Sci. Technol.* 52 (23), 13681–13689. <https://doi.org/10.1021/acs.est.8b04367>. Doi:
- Leecaster, K., Ayling, B., Moffitt, G., Rose, P.E., 2012. Use of safranin T as a reactive tracer for geothermal reservoir characterization. In: *Proceedings, 37th Workshop on Geothermal Reservoir Engineering* Stanford University.
- Lei, T., Chuo, R., Zhao, J., Shi, X., Liu, L., 2010. An improved method for shallow water flow velocity measurement with practical electrolyte inputs. *J. Hydrol. (Amst)* 390 (1–2), 45–56. <https://doi.org/10.1016/j.jhydrol.2010.06.029>.
- Leij, F.J., Toride, N., van Genuchten, M.Th., 1993. Analytical solutions for non-equilibrium solute transport in three-dimensional porous media. *J. Hydrol. (Amst)* 151 (2–4), 193–228. [https://doi.org/10.1016/0022-1694\(93\)90236-3](https://doi.org/10.1016/0022-1694(93)90236-3) doi.org/.
- Leij, F.J., Priesack, E., Schaap, Marcel, G., 2000. Solute transport modeled with green's functions with application to persistent solute sources. *J. Contam. Hydrol.* 41 (1–2), 155–173. [https://doi.org/10.1016/S0169-7722\(99\)00062-5](https://doi.org/10.1016/S0169-7722(99)00062-5) doi.org/.
- Li, X., Wen, Z., Zhan, H., Wu, F., Zhu, Q., 2021. Laboratory observations for two-dimensional solute transport in an aquifer-aquitard system. *Environ. Sci. Pollut. Res.* 1–15. <https://doi.org/10.1007/s11356-021-13123-1>.
- Maloszewski, P., Zuber, A., 1985. On the theory of tracer experiments in fissured rocks with a porous matrix. *J. Hydrol. (Amst)* 79 (3–4), 333–358. [https://doi.org/10.1016/0022-1694\(85\)90064-2](https://doi.org/10.1016/0022-1694(85)90064-2).
- Maloszewski, P., Zuber, A., 1985. On the theory of tracer experiments in fissured rocks with a porous matrix. *Journal of Hydrology* 79 (3–4), 333–358. [https://doi.org/10.1016/0022-1694\(85\)90064-2](https://doi.org/10.1016/0022-1694(85)90064-2).
- Molina-Giraldo, N., Blum, P., Zhu, K., Bayer, P., Fang, Z., 2011a. A moving finite line source model to simulate borehole heat exchangers with groundwater advection. *Int. J. Therm. Sci.* 50 (12), 2506–2513. <https://doi.org/10.1016/j.ijthermalsci.2011.06.012>.
- Molina-Giraldo, N., Bayer, P., Blum, P., 2011b. Evaluating the influence of thermal dispersion on temperature plumes from geothermal systems using analytical solutions. *Int. J. Therm. Sci.* 50 (7), 1223–1231. <https://doi.org/10.1016/j.ijthermalsci.2011.02.004>.
- MATLAB (2021). <https://www.mathworks.com/help/matlab/programming-and-data-types.html>, accessed on 04/01/2021.
- Neuman, S.P., 1987. Stochastic continuum representation of fractured rock permeability as an alternative to the REV and fracture network concepts. In: *Rock Mechanics: Proceedings of the 28th U.S. Symposium*, Tucson, Arizona, edited by I. W. Farmer, pp. 533–561, A. A. Balkema, Rotterdam, p. 1240. [https://doi.org/10.1007/978-94-009-2889-3\\_19](https://doi.org/10.1007/978-94-009-2889-3_19).
- Neuman, S.P., 1990. Universal scaling of hydraulic conductivities and dispersivities in geologic media. *Water Resour. Res.* 26 (8), 1749–1758. <https://doi.org/10.1029/WR026i008p01749>.
- Neuman, S.P., 1994. Generalized scaling of permeabilities: validation and Effect of upscale choice. *Geophys. Res. Lett.* 21 (5), 349–352. <https://doi.org/10.1029/94GL00308>.
- Neuman, S.P., 2005. Trends, prospects and challenges in quantifying flow and transport through fractured rocks. *Hydrogeol. J.* 13 (1), 124–147. <https://doi.org/10.1007/s10040-004-0397-2>.
- Neuman, S.P., 2008. Multiscale relationships between fracture length, aperture, density and permeability. *Geophys. Res. Lett.* L22402. <https://doi.org/10.1029/2008GL035622>.
- Neuman, S.P., Di Federico, V., 2003. Multifaceted nature of hydrogeologic scaling and its interpretation. *Rev. Geophys.* 41 (3), 1014. <https://doi.org/10.1029/2003RG000130>.
- Neuman, S.P., 2016. Comment on “Is unique scaling of aquifer macrodispersivity supported by field data?” by A. Zech et al. *Water Resour. Res.* 52, 4199–4202. <https://doi.org/10.1002/2016WR018636>.
- Park, B.-H., Lee, K.-K., 2021. Evaluating anisotropy ratio of thermal dispersivity affecting geometry of plumes generated by aquifer thermal use. *J. Hydrol. (Amst)*. <https://doi.org/10.1016/j.jhydrol.2021.126740>.
- Pruess, K., 1992. *Brief Guide to the MINC-Method For Modeling Flow and Transport in Fractured Media*. LBL-32195. Lawrence Berkeley Laboratory, Berkeley, California.
- Rivera, J.A., Blum, P., Bayer, P., 2016a. Influence of spatially variable ground heat flux on closed-loop geothermal systems: line source model with nonhomogeneous Cauchy-type top boundary conditions. *Appl. Energy* 180, 572–585. <https://doi.org/10.1016/j.apenergy.2016.06.074>.
- Rivera, J.A., Blum, P., Bayer, P., 2016b. A finite line source model with cauchy-type top boundary conditions for simulating near surface effects on borehole heat exchangers. *Energy* 98, 50–63. <https://doi.org/10.1016/j.energy.2015.12.129>.
- Ronchetti, F., Piccinini, L., Deiana, M., Ciccarese, G., Vincenzi, V., Aguzzoli, A., Malavasi, G., Fabbri, P., Corsini, A., 2020. Tracer test to assess flow and transport parameters of an earth slide: the Montecagno landslide case study (Italy). *Eng. Geol.* 275, 105749 <https://doi.org/10.1016/j.enggeo.2020.105749>.
- Rose, P.E., Johnson, S.D., Kilbourn, P., Kasteler, C., 2002. Tracer testing at Dixie Valley, Nevada using 1-naphthalene sulfonate and 2,6-naphthalene disulfonate. In: *Proceedings, Twenty-Seventh Workshop on Geothermal Reservoir Engineering*, Stanford University, Stanford, California, January 28–30, 2002. SGP-TR-171.
- Rose, P.E., Benoit, W.R., Kilbourn, P.M., 2001. The application of the polyaromatic sulfonates as tracers in geothermal reservoirs. *Geothermics* 30 (6), 617–640. [https://doi.org/10.1016/S0375-6505\(01\)00024-4](https://doi.org/10.1016/S0375-6505(01)00024-4) doi.org/.
- Rose, P.E., Clausen, S., 2014. The Use of Amino G as a Thermally Reactive Tracer for Geothermal Applications. In: *Proceedings, 39th Workshop on Geothermal Reservoir Engineering* Stanford University, pp. 1–5.
- Rose, P.E., Clausen, S., 2017. The use of amino-substituted naphthalene sulfonates as tracers in geothermal reservoirs. In: *Proceedings, 42nd Workshop on Geothermal Reservoir Engineering*, Stanford University, pp. 1–7.
- Rostami, P., Sharifi, M., Dejam, M., 2020. Shape factor for regular and irregular matrix blocks in fractured porous media. *Pet. Sci.* 17, 136–152. <https://doi.org/10.1007/s12182-019-00399-9>.

- Roubinet, D., de Dreuzay, J.-R., Tartakovsky, D.M., 2012. Semi-analytical solutions for solute transport and exchange in fractured porous media. *Water Resour Res* 48, W01542. <https://doi.org/10.1029/2011WR011168>.
- Sauty, J.-P., 1980. An analysis of hydrodispersive transfer in aquifers. *Water Resour Res* 16 (1), 145–158. <https://doi.org/10.1029/WR016i001p00145>.
- Somogyvári, M., Bayer, P., 2017. Field validation of thermal tracer tomography for reconstruction of aquifer heterogeneity. *Water Resour Res* 53 (6), 5070–5084. <https://doi.org/10.1002/2017WR020543>.
- Şimşek, Ş., 2003. Hydrogeological and isotopic survey of geothermal fields in the Buyuk Menderes graben, Turkey. *Geothermics* 32, 669–678. [https://doi.org/10.1016/S0375-6505\(03\)00072-5](https://doi.org/10.1016/S0375-6505(03)00072-5) doi.org/.
- Şimşek, Ş., Yıldırım, N., Gülgör, A., 2005. Developmental and environmental effects of the Kizildere geothermal power project, Turkey. *Geothermics* 34 (2), 234–251. <https://doi.org/10.1016/j.geothermics.2004.12.005>.
- Tang, D.W.S., van der Zee, S.E.A.T.M., 2021. Dispersion and recovery of solutes and heat under cyclic radial advection. *J. Hydrol. (Amst)* 602, 126713. <https://doi.org/10.1016/j.jhydrol.2021.126713>.
- Tómasdóttir, S., 2018. MSc. Thesis. Uppsala University, Sweden.
- TOUGH2 (2021), <https://tough.lbl.gov/software/tough/> accessed at 04/01/2021.
- van Genuchten, M.Th., Alves, W.J., 1982. Analytical solutions of the one-dimensional convective-dispersive solute transport equation. *Techn. Bull., United States Depart. Agricul.* 1661.
- van Genuchten, M.Th., 1985. A general approach for modeling solute transport in structured soils. *Memor. Intern. Assoc. Hydrogeol.* 17 (2), 513–526.
- van Genuchten, M.Th., Dalton, F.N., 1986. Models for simulating salt movement in aggregated field soils. *Geoderma* 38, 165–183. [https://doi.org/10.1016/0016-7061\(86\)90013-3](https://doi.org/10.1016/0016-7061(86)90013-3) doi.org/.
- Warren, J.E., Root, P.J., 1963. The behavior of naturally fractured reservoirs. *Soc. Pet. Eng. J.* 228, 245–255. [doi.org/10.2118/426-PA](https://doi.org/10.2118/426-PA).
- Wu, H., Fu, P., Morris, J.P., Mattson, E.D., Neupane, G., Smith, M.M., Hawkins, A.J., Zhang, Y., Kneafsey, T., EGS Collab Team, 2021. Characterization of flow and transport in a fracture network at the EGS Collab field experiment through stochastic modeling of tracer recovery. *J. Hydrol. (Amst)* 593, 125888. <https://doi.org/10.1016/j.jhydrol.2020.125888>.
- Yadav, R.R., Roy, J., 2018. Solute transport phenomena in a heterogeneous semi-infinite porous media: an analytical solution. *Intern. J. Appl. Computation. Mathe.* 4, 135. <https://doi.org/10.1007/s40819-018-0567-x>.
- Zhang, S., Tullis, T.E., Scruggs, V.J., 1999. Permeability anisotropy and pressure dependency of permeability in experimentally sheared gouge materials. *J. Struct. Geol.* 21 (7), 795–806. [https://doi.org/10.1016/S0191-8141\(99\)00080-2](https://doi.org/10.1016/S0191-8141(99)00080-2).
- Zech, A., Attinger, S., Cvetkovic, V., Dagan, G., Dietrich, P., Fiori, A., Rubin, Y., Teutsch, G., 2015. Is unique scaling of aquifer macrodispersivity supported by field data? *Water Resour. Res.* 51, 7662–7679. <https://doi.org/10.1002/2015WR017220>.